

¹ Susceptible host dynamics explain pathogen resilience
²

³

⁴ Sang Woo Park, . . . , Sarah Cobey

⁵ **Abstract**

⁶ Major priority for epidemiological research in the time of anthropogenic change is
⁷ understanding how infectious disease dynamics respond to perturbations. Interven-
⁸ tions to slow the spread of COVID-19 significantly disrupted the transmission of
⁹ other human pathogens, providing unique opportunities to learn about pathogen
¹⁰ characteristics from spatiotemporal variation in re-emergence patterns. As inter-
¹¹ ventions lifted, a key question of whether and when respiratory pathogens would
¹² eventually return to their pre-pandemic dynamics remains to be answered. To ad-
¹³ dress this gap, we develop a framework for estimating pathogen resilience based on
¹⁴ how fast epidemic patterns return to their pre-pandemic, endemic dynamics. Our
¹⁵ analysis reveals a possibility that some pathogens may have settled to endemic cycles
¹⁶ that are different from their pre-pandemic patterns. Finally, we show that the re-
¹⁷ plenishment rate of the susceptible pool is a key determinant of pathogen resilience.
¹⁸ Our framework offers a novel perspective to characterizing the dynamics of endemic
¹⁹ pathogens and their responses to COVID-19 interventions.

Understanding how ecological systems respond to perturbations is a fundamental challenge in predicting species persistence and extinction [1, 2, 3]. These responses can be characterized in terms of resilience, which often measures how fast a system returns to its stable, reference state following a perturbation [4, 5, 6, 7]. Both theoretical and empirical efforts to quantify resilience of ecological systems have provided key insights for understanding the dynamics of complex systems and linking these findings to actionable strategies for species conservation [8]. However, despite rich literature on ecological resilience, there have been limited applications to measuring the resilience of host-pathogen systems, especially for human pathogens.

Non-pharmaceutical interventions (NPIs) to slow the spread of COVID-19 disrupted the transmission of other human pathogens, providing large-scale natural experiments for understanding how various host-pathogen systems respond to perturbations [9, 10, 11, 12]. In particular, as interventions lifted, large heterogeneities in outbreak dynamics were observed across different pathogens in different countries (Figure 1), likely reflecting differences in NPI patterns, pathogen characteristics, immigration/importation from other countries, and pre-pandemic pathogen dynamics [13]. Even though more than four years have already passed since the emergence of COVID-19, current circulation patterns for many respiratory pathogens appear to be different from their pre-pandemic, seasonal patterns, especially in Hong Kong and Korea: some pathogens, such as human metapneumovirus and bocavirus in Korea, are circulating at lower levels, whereas other pathogens, such as RSV in Korea, seem to exhibit different seasonality (Figure 1). These observations pose two fundamental questions for current and future infectious disease dynamics: (1) can we learn about underlying pathogen characteristics, such as their transmissibility or duration of immunity, from re-emergence patterns? and (2) can we predict whether and when other respiratory pathogens will eventually return to their pre-pandemic dynamics?

To address this question, we propose a framework for characterizing the resilience of a host-pathogen system based on how fast the system recovers from perturbation. We begin by laying out a few representative scenarios that capture the potential impact of COVID-19 interventions on endemic pathogen dynamics and illustrating how resilience can be measured by comparing the pre- and post-pandemic dynamics of susceptible and infected hosts. In practice, information on susceptible hosts are often unavailable, and traditional methods for reconstructing the dynamics of susceptible hosts require long-term endemic time series [14, 15], which cannot be applied due to disruptions in epidemic patterns caused by COVID-19 interventions. Instead, we utilize Takens' embedding theorem to reconstruct empirical attractors from data and further measure the distance from this empirical attractor [16]. This reconstruction allows us to characterize the rate at which this distance decreases over time, which correspond to pathogen resilience. We apply this framework to analyzing pathogen surveillance data for a wide array of respiratory and non-respiratory pathogens from Canada, Hong Kong, Korea, and US. Finally, we show that susceptible host dynamics are a key determinants of pathogen resilience. Our study offers unique insights into understanding pathogen re-emergence patterns following COVID-19 interventions.

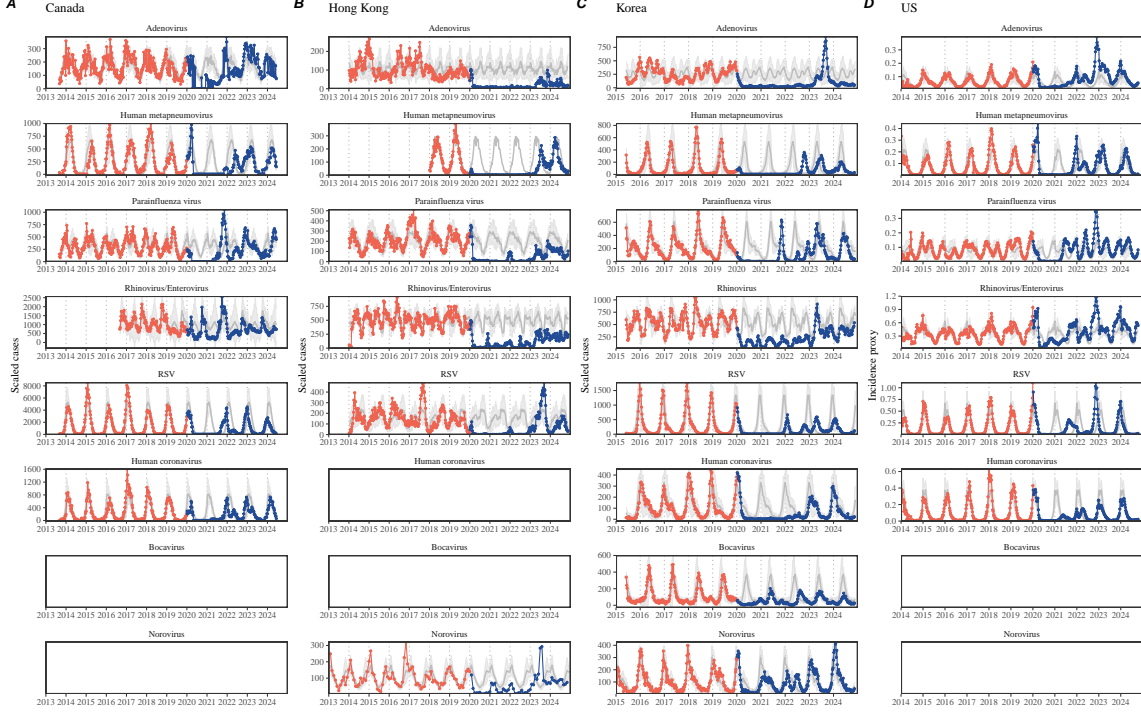


Figure 1: **Observed heterogeneity in responses to COVID-19 pandemic across respiratory pathogens and norovirus in (A) Canada, (B) Hong Kong, (C) Korea, and (D) US.** Red points and lines represent data before 2020. Blue points and lines represent data since 2020. Gray lines and shaded regions represent the mean seasonal patterns and corresponding 95% confidence intervals based on the observed outbreak patterns before 2020.

63 Conceptual introduction to pathogen resilience

64 In classical ecological literature, resilience of an ecological system is measured by
 65 the rate at which the system returns to its reference state following a perturbation
 66 [4, 5, 6, 7]. This rate corresponds to the largest real part of the eigenvalues of the
 67 linearized system near equilibrium—here, we refer to this value as the *intrinsic* re-
 68 silience of the system, which represents the expected rate of return from perturbed
 69 states. However, respiratory pathogens often exhibit seasonal variation in transmis-
 70 sion, meaning that the intrinsic resilience of a host-pathogen system varies across
 71 season. Nonetheless, we can still measure the *empirical* resilience of a host-pathogen
 72 system by looking at how fast the system returns to the pre-pandemic, endemic
 73 dynamics after interventions are lifted.

74 As an example, consider an intervention that reduce transmission by 50% for 6
 75 months starting in 2020, which causes epidemic patterns to deviate from its original
 76 stable annual cycle for a short period of time and eventually come back (Figure 2A).
 77 To measure the empirical resilience of this system, we first need to be able to measure

78 the distance from its pre-pandemic attractor. There are many different ways we can
79 measure the distance from attractor, but for illustrative purposes, we choose one of
80 the most parsimonious approach: that is, we look at how the susceptible (S) and
81 infected (I) populations change over time and measure the distance on the SI phase
82 plane (Figure 2B). In this simple case, the locally estimated scatterplot smoothing
83 (LOESS) fit indicates that the distance from attractor decreases linearly on average
84 (Figure 2C). Furthermore, the overall rate of return matches the intrinsic resilience
85 of the seasonally unforced system (Figure 2C).

86 Alternatively, NPIs can permanently change our behavior and have persisting
87 impact on the pathogen dynamics; as an example, we consider a scenario in which a
88 10% reduction in transmission persists even after the NPIs are lifted (Figure 2D–F).
89 In such cases, we cannot know whether the pathogen will return to its original cycle
90 or a different cycle until many years have passed after the NPIs are lifted, meaning
91 that we cannot measure the distance against the new attractor that the system will
92 eventually approach. Nonetheless, we can still measure the distance against the orig-
93 inal, pre-pandemic attractor and ask how the distance changes over time (Figure 2E).
94 The LOESS fit suggests that the distance from the attractor will initially decrease
95 exponentially on average (equivalently, linearly on a log scale) and eventually plateau
96 (Figure 2F). Here, a permanent 10% reduction in transmission rate slows down the
97 system, which causes the distance from the attractor to decrease at a slower rate
98 (Figure 2F) than it would have otherwise in the absence of permanent transmission
99 reduction (Figure 2C). This example shows that resilience is not necessarily an in-
100 trinsic property of a specific pathogen. Instead, pathogen resilience is a property of
101 a specific attractor that a host-pathogen system approaches, which depends on both
102 pathogen and host characteristics.

103 Finally, transient phenomena can also complicate the picture (Figure 2G–I). For
104 example, a stage-structured model for RSV initially exhibits a stable annual cycle,
105 but perturbations from NPIs cause the epidemic to exhibit biennial cycles (Figure
106 2G). Despite this biennial cycle, we see that the system eventually approaches the
107 original pre-pandemic attractor (Figure 2H), suggesting that this biennial cycle is a
108 transient phenomenon. The LOESS fit indicates that the distance from the attractor
109 will initially decrease exponentially at a rate that is consistent with the intrinsic
110 resilience of the seasonally unforced system, but the rate of decrease slows down
111 as the epidemic exhibits a biennial cycle (Figure 2I). In classical ecological theory,
112 this behavior is also referred to as a ghost attractor, which causes long transient
113 dynamics and slow transitions [17]. As we show in Supplementary Figure S1, strong
114 seasonal forcing in transmission can also lead to transient phenomena for a simple
115 SIRS model, causing a slowing down of the system.

116 In Supplementary Materials, we also explore measuring the resilience of a two-
117 strain host-pathogen system: when the dynamics two strains (or two pathogens) are
118 coupled through cross immunity, we would expect the entire system to be character-
119 ized by a single resilience value (rather than having two separate resilience for each
120 strain). Simulations from a simple two-strain system illustrate that separate anal-

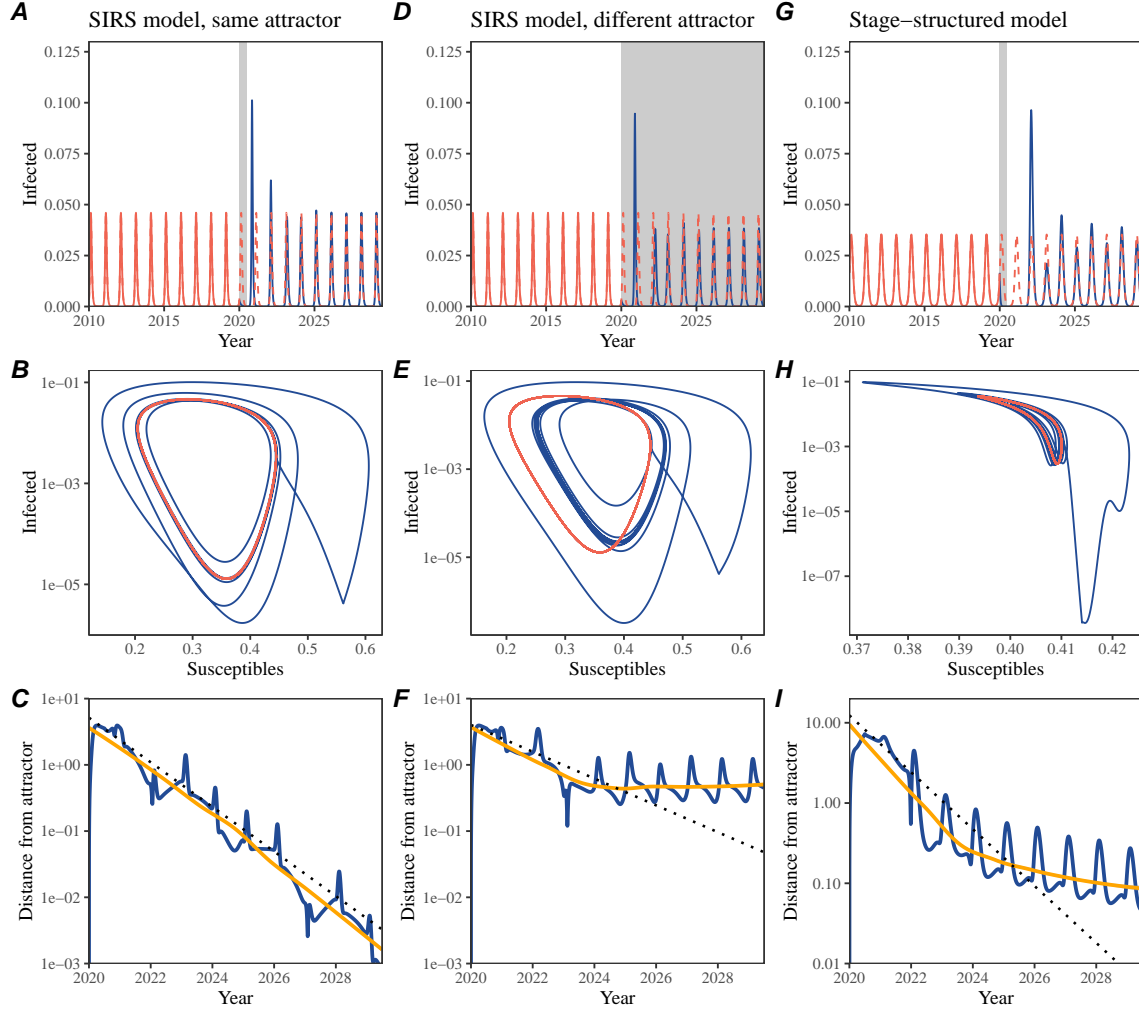


Figure 2: Conceptual framework for measuring pathogen resilience following NPIs across different scenarios. (A, D, G) Simulated epidemic trajectories across various models. Red and blue solid lines represent epidemic dynamics before and after interventions are introduced, respectively. Red dashed lines represent counterfactual epidemic dynamics in the absence of interventions. Gray regions indicate the duration of interventions. (B, E, H) Phase plane representation of the corresponding model. Red and blue solid lines represent epidemic trajectories on an SI phase plane before and after interventions are introduced, respectively. (C, F, I) Changes in logged distance from attractor over time. Blue lines represent the logged distance from attractor. Orange lines represent the locally estimated scatterplot smoothing (LOESS) fits to the logged distance from attractor. Dotted lines are superimposed as a comparison to have the same slope as the intrinsic resilience of the seasonally unforced system.

yses of individual strain dynamics (e.g., RSV A vs B) and a joint analysis of total

122 infections (e.g., total RSV infections) yield identical resilience estimates, confirming
123 our expectation (Supplementary Figure S2, 3). Analogous to a single system, strong
124 seasonal forcing in transmission can cause the system to slow down through transient
125 phenomena (Supplementary Figure S4).

126 These observations indicate three possibilities. First, we can directly estimate
127 the empirical resilience of a host-pathogen system by looking at how fast the system
128 approaches a pre-pandemic attractor, provided that we can measure the distance
129 from attractor. The empirical approach to estimating pathogen resilience is partic-
130 ularly convenient because it does not require us to know the true underlying model.
131 As we show in Supplementary Figure S5, estimating the intrinsic resilience from fit-
132 ting standard compartmental models can lead to biased estimates, especially under
133 model misspecification. Second, resilience estimates allow us to make phenomenolog-
134 ical predictions about the dynamics of a host-pathogen system following a perturba-
135 tion: assuming that the distance from the attractor will decrease exponentially over
136 time, we can obtain a ballpark estimate for when the system will reach an attractor.
137 Finally, deviation from an exponential decrease in the distance from attractor can
138 provide information about whether the system has reached an alternative attractor,
139 or a ghost attractor, that is different from the original, pre-pandemic attractor. These
140 alternative attractors may reflect continued perturbations from permanent changes
141 in transmission patterns as well as changes in immune landscapes.

142 **Inferring pathogen resilience from real data**

143 Based on these observations, we now set out to infer pathogen resilience from real
144 data. Here, we briefly lay out our approach to estimating pathogen resilience from
145 real data (Figure 3). We then test this approach against simulations and apply it to
146 real data.

147 So far, we focused on simple examples that assume a constant transmission re-
148 duction. However, in practice, the impact of NPIs on pathogen transmission is
149 likely more complex (Figure 3A), reflecting introduction and relaxation of various
150 intervention strategies. These complexities can lead to longer delays between the
151 introduction of NPIs and pathogen re-emergence as well as temporal variation in
152 outbreak sizes (Figure 3B): in this example, continued transmission reduction from
153 NPIs limits the size of the first outbreak in 2021 following the emergence, allowing
154 for a larger outbreak in 2022 when NPIs are further relaxed.

155 Previously, we relied on the dynamics of susceptible and infected hosts to compute
156 the distance from attractor (Figure 2), but information on susceptible hosts are
157 often not available in practice. In addition, uncertainties in case counts due to
158 observation error as well as the possibility of complex, multiannual attractor adds
159 challenges to measuring the distance from attractor. To address these challenges, we
160 first reconstruct an empirical attractor by utilizing Takens' theorem, which states
161 that an attractor of a nonlinear multidimensional system can be mapped onto a

162 delayed embedding [16]. Here, we use delayed copies of logged values of pre-pandemic
 163 cases $C(t)$ (Figure 3C) to reconstruct the attractor:

$$\langle \log(C(t) + 1), \log(C(t - \tau) + 1), \dots, \log(C(t - (M - 1)\tau) + 1) \rangle, \quad (1)$$

164 where the delay τ and embedding dimension M are determined based on autocor-
 165 relations and false nearest neighbors, respectively [18, 19]. We then apply the same
 166 delay and embedding dimensions to the entire time series to determine the position
 167 on a multi-dimensional state space (Figure 3D), which allows us to measure the
 168 nearest neighbor distance between the current state of the system and the empirical
 169 attractor (Figure 3E). In principle, we can quantify how fast this distance decreases
 170 by fitting a linear regression on a log scale, where the slope of the linear regression
 171 corresponds to pathogen resilience. As we show in Supplementary Figure S6, over-
 172 all temporal variations in the distance from attractor, especially the observed rate
 173 of decrease, appear robust to choices about embedding delays and dimensions; we
 174 note that using longer delays and higher dimensions tend to smooth out temporal
 175 variations in the distance from attractor.

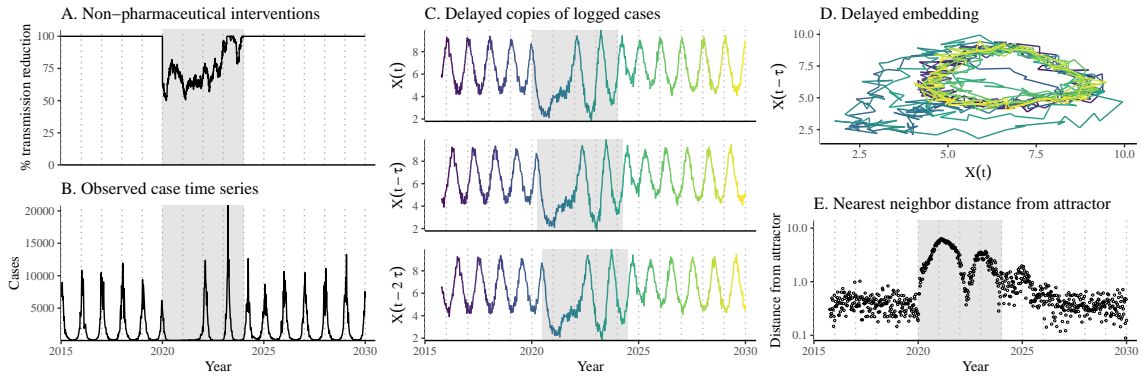


Figure 3: **A schematic diagram explaining how pathogen resilience can be inferred from real data.** (A) A realistic example of a synthetic NPI, represented by a relative reduction in transmission. (B) The impact of the synthetic NPI on epidemic dynamics simulated using a stochastic SIRS model. (C) Generating delayed copies of the logged time series allows us to obtain an embedding. (D) Two dimensional representation of an embedding. (E) Delayed embedding allows us to calculate the nearest neighbor distance from the empirical attractor, which is determined based on the pre-pandemic time series. This distance time series can be used to infer pathogen resilience by fitting a linear regression after choosing an appropriate window for regression.

176 Complex changes in the distance from attractor suggest that estimating pathogen
 177 resilience from linear regression will likely be sensitive to our choice of fitting windows
 178 for the regression. In Supplementary Materials, we explore an automated window
 179 selection criteria for linear regression and test it against randomized, stochastic sim-
 180 ultations across a wide range of realistic NPI shapes. We find that resilience estimates

181 based on the automated window selection criteria are moderately correlated (0.54)
182 with the intrinsic resilience of the post-NPI attractor (Supplementary Figure S7). In
183 contrast, a naive approach that uses the entire time series, starting from the peak
184 distance, only gives a correlation of 0.21 and consistently underestimates the intrinsic
185 resilience (Supplementary Figure S7).

186 Now, we apply this approach to pathogen surveillance data presented in Figure
187 1. For each time series, we apply Takens' theorem independently to reconstruct the
188 empirical attractor and obtain the corresponding time series of distance from attrac-
189 tors (Supplementary Figure S8 for the distance time series and linear regression fits).
190 Then, we use the automated window selection criteria to fit a linear regression and
191 estimate the empirical resilience for each pathogen in each country. For most res-
192 piratory pathogens, resilience estimates fall between 0.4/year and 1.8/year (Figure
193 4A), with the exception of Rhinovirus in the US (0.066/year; 95% CI: 0.018/year–
194 0.113/year) and Bocavirus in Korea (0.087/year; 95% CI: 0.023/year–0.151/year).
195 Excluding these exceptions, the mean resilience of common respiratory pathogens is
196 0.974/year (95% CI: 0.784/year–1.16/year). As a reference, this is \approx 7 times higher
197 than the intrinsic resilience of pre-vaccination measles dynamics (\approx 0.13/year). Fi-
198 nally, resilience estimates for norovirus appears to be comparable to the intrinsic
199 resilience of measles: 0.119/year (95%CI: 0.004/year–0.233/year) for Korea and
200 0.385/year (95% CI: 0.167/year–0.603/year). A simple ANOVA shows that there
201 are significant differences in resilience estimates across countries ($p < 0.036$) and
202 pathogens ($p < 0.030$).

203 Using resilience estimates, we now predict when each pathogen will return to
204 their original pre-pandemic cycles. Specifically, we extend our linear regression fits
205 to distance-from-attractor time series and ask when the predicted regression line
206 will cross a threshold value, which we set to a mean of pre-pandemic distances. We
207 predict that a return to pre-pandemic cycles would be imminent for most pathogens
208 (Figure 4B; see Supplementary Figure S9 for a zoomed out version). In addition, we
209 also predict that many pathogens should have already returned to their pre-pandemic
210 dynamics by the end of 2024; but these predictions contradict some of the observed
211 pathogen dynamics. For example, we predict that both human metapneumovirus and
212 RSV in Korea should have returned to their attractors by now, but the magnitude
213 and timing of recent epidemics are different from pre-pandemic patterns (Figure 1).
214 These observations suggest the possibility that some common respiratory pathogens
215 may have converged to different attractors.

216 In Supplementary Materials, we also consider using a lower threshold for the false
217 nearest neighbor approach when determining the embedding dimension; this gives
218 a higher embedding dimension. As explained earlier (Supplementary Figure S6),
219 this gives a smoother distance-from-attractor time series (compare Supplementary
220 Figure S10 with S8); this also requires us to use longer time series, which prevents
221 us from estimating resilience for some pathogens. Overall, resulting estimates of
222 pathogen resilience with higher embedding dimensions still fall between 0.3/year
223 and 2.1/year for the most part (Supplementary Figure S11). A direct comparison

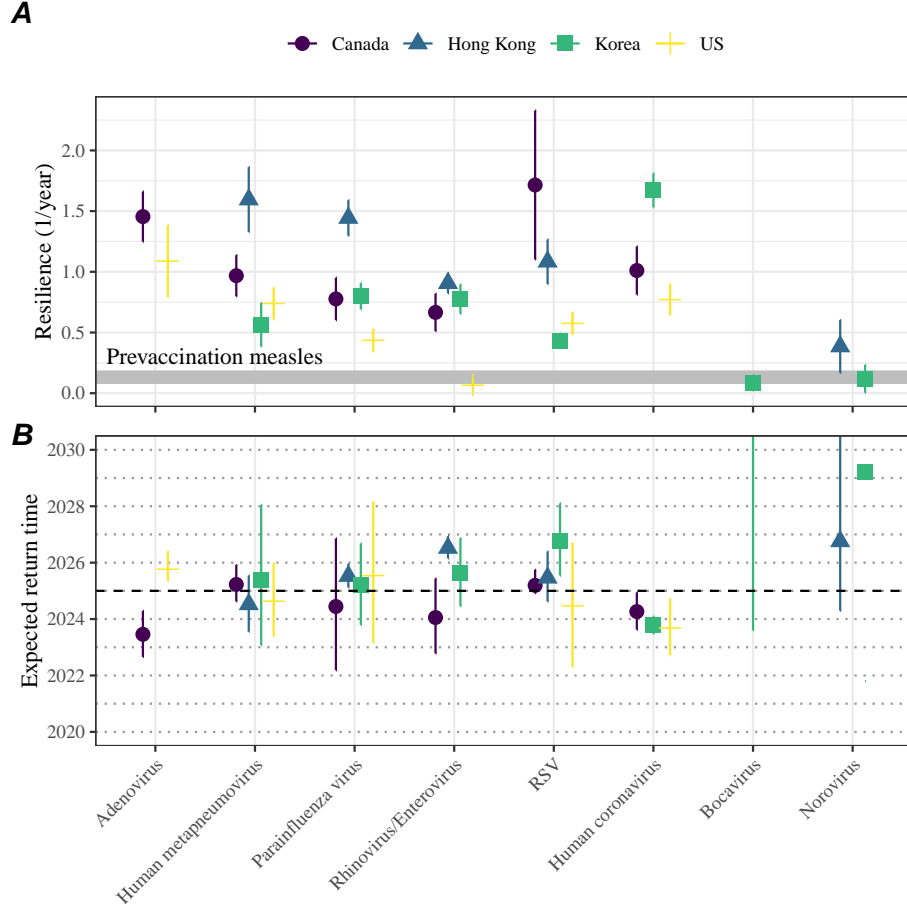


Figure 4: **Summary of resilience estimates.** (A) Estimated pathogen resilience. The gray horizontal line represents the intrinsic resilience of pre-vaccination measles dynamics. (B) Predicted timing of when each pathogen will return to their pre-pandemic cycles. The dashed line in panel B indicates the end of 2024 (current observation time). Error bars represent 95% confidence intervals.

²²⁴ between two approaches (i.e., original estimate vs using higher dimensions) shows a
²²⁵ strong consistency in resilience estimates (Supplementary Figure S12).

²²⁶ Susceptible host dynamics explain variation in pathogen ²²⁷ resilience

²²⁸ So far, we focused on quantifying pathogen resilience from the observed patterns of
²²⁹ pathogen re-emergence following COVID-19 interventions. But what factors deter-
²³⁰ mine how resilient a host-pathogen system is? Here, we use a standard Susceptible-
²³¹ Infected-Recovered-Susceptible (SIRS) model to show that susceptible host dynamics

232 are the key determinants of pathogen resilience. To do so, we vary the basic reproduction
 233 number \mathcal{R}_0 , which represents the average number of secondary infections caused
 234 by a newly infected individual in a fully susceptible population, and the duration of
 235 immunity and compute intrinsic resilience for each parameter.

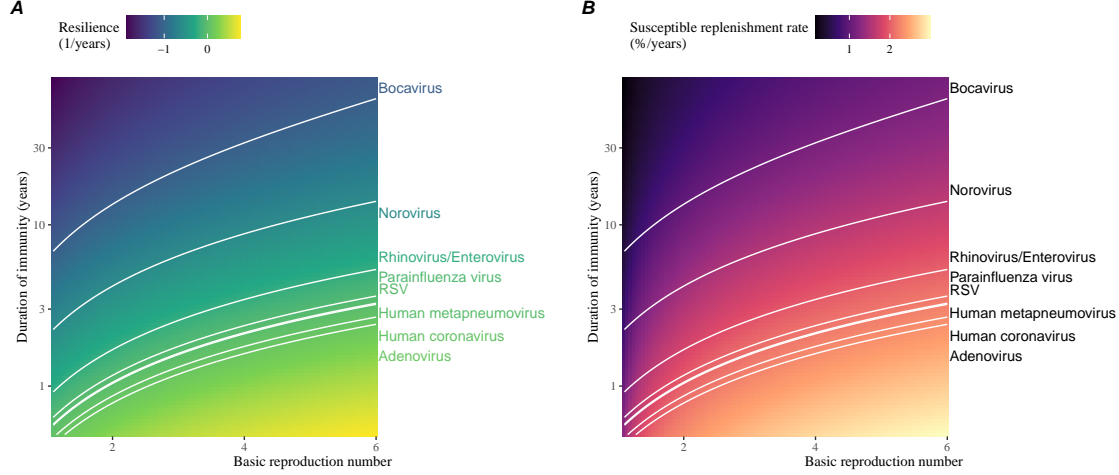


Figure 5: **Linking pathogen resilience to epidemiological parameters and susceptible host dynamics.** (A) The heat map represents intrinsic resilience as a function of the basic reproduction number \mathcal{R}_0 and the duration of immunity. (B) The heat map represents per-capita susceptible replenishment rate as a function of the basic reproduction number \mathcal{R}_0 and the duration of immunity. The standard SIRS model is used to compute intrinsic resilience and per-capita susceptible replenishment rate. Lines correspond to a set of parameters that are consistent with mean resilience estimates for each pathogen. Pathogens are ranked based on their mean resilience estimates, averaged across different countries.

236 We find an increase in \mathcal{R}_0 and a decrease in duration of immunity correspond
 237 to an increase in pathogen resilience (Figure 5A). These variations can be under-
 238 stood in terms of the susceptible host dynamics, where faster per-capita susceptible
 239 replenishment rate causes the system to be more resilient (Figure 5B). This rate can
 240 be expressed as a ratio between absolute rate at which new susceptibles enter the
 241 population and the equilibrium number of susceptible individuals in the population,
 242 \bar{S} . Therefore, both higher \mathcal{R}_0 and shorter duration of immunity can drive faster
 243 per-capita susceptible replenishment rate (Figure 5B), especially because higher \mathcal{R}_0
 244 leads to lower \bar{S} .

245 Finally, we can now rank different pathogens based on the average values of em-
 246 pirical resilience, which allows us to determine a set of parameters that are consistent
 247 with the estimated resilience (Figure 5A). Across all pathogens we consider, except
 248 for bocavirus and norovirus, we estimate that the average duration of immunity is
 249 likely to be short (< 6 years) across a plausible range of \mathcal{R}_0 . These rankings further

allow us to map each pathogen onto a set of parameters that are consistent with its empirical resilience (Figure 5A) and obtain a plausible range of susceptible replenishment rates for each pathogen (Figure 5B). However, we note that there is no one-to-one correspondence between susceptible replenishment rates and pathogen resilience, leading to a wide uncertainty in the estimates for susceptible replenishment rates (Figure 5B).

Discussion

The COVID-19 interventions have caused major disruptions to circulation patterns of both respiratory and non-respiratory pathogens, adding challenges to predicting their future dynamics [9, 10, 11, 12]. On the other hand, these interventions offer large-scale natural experiments for understanding how different pathogens respond to perturbations. In this study, we show that pathogen re-emergence patterns following COVID-19 interventions can be characterized through the lens of ecological resilience. Traditionally, ecological resilience measures how fast a system returns to a reference state following a perturbation. In the context of respiratory pathogens, resilience measures how fast epidemics return to their endemic cycles after interventions are lifted.

We use an attractor reconstruction approach to quantify how distance from attractor changes over time for each pathogen [16]. We show that the resilience of a host-pathogen system can be estimated by fitting a linear regression to a logged distance-from-attractor time series. Overall, we estimate that the resilience for most common respiratory pathogens ranges between 0.4/year and 1.8/year, which is 3–14 times more resilient than prevaccination measles, indicating potential challenges in controlling common respiratory pathogens.

Our framework allows us to make phenomenological predictions about when each pathogen will return to their endemic cycles. The ability to predict future epidemic patterns from resilience estimates offers a new paradigm for epidemic forecasting. While this approach cannot predict the exact timing of outbreaks or epidemic patterns, it is nonetheless useful for predicting when epidemics will settle down to regular cycles after a large perturbation, such as COVID-19 interventions.

Our analyses suggest a possibility that several pathogens may have converged to different endemic cycles compared to their pre-pandemic epidemic patterns. Key examples include human metapnuemovirus, RSV, and bocavirus in Korea as well as RSV in Hong Kong. These changes may reflect changes in surveillance or actual shift in the dynamics, caused by permanent changes in behavior or population-level immunity. While it seems unlikely that permanent changes in behavior would only affect a few pathogens and not others, we cannot rule out this possibility given heterogeneity in the age of infection across different respiratory pathogens [SWP: CITE]. A shift in population-level immunity is plausible, as the emergence of SARS-CoV-2 and extinction of influenza B/Yamagata likely caused major changes in immune landscapes;

290 interactions among co-circulating pathogens, such as cross immunity between RSV
291 and HMPV [20], may have also contributed to changes in population-level immu-
292 nity. However, we currently do not know how immunity, or lack thereof, from these
293 pathogens would affect infection from other pathogens. Future studies should use
294 detailed mechanistic models, coupled with behavioral and immunological data, to
295 test these hypotheses and better understand post-pandemic dynamics of endemic
296 pathogens.

297 We show that susceptible host dynamics shape pathogen resilience, where faster
298 replenishment of the susceptible population causes the pathogen to be more resilient.
299 For simplicity, we focus on waning immunity and birth as a main driver of the suscep-
300 tible host dynamics but other mechanisms can also contribute to the replenishment
301 of the susceptible population. In particular, pathogen evolution, especially the emer-
302 gence of antigenically novel strains, can cause effective waning of immunity in the
303 population; therefore, we hypothesize that faster rates of antigenic evolution can also
304 cause a pathogen to be more resilient. Future studies should explore the relationship
305 between the rate of evolution and resilience for antigenically evolving pathogens.

306 Quantifying pathogen resilience also offers novel approaches to validating population-
307 level epidemiological models. So far, the majority of model validation in epidemiology
308 is based on the ability of a model to reproduce the observed epidemic dynamics and
309 to predict future dynamics [21, 20, 22, 23, 24]. However, there can be plethora of
310 models that meet these criteria. For example, two major RSV models have been pro-
311 posed so far to explain biennial epidemic patterns: (1) a stage- and age-structured
312 model that allows for disease severity to vary with number of past infections and
313 age of infection [22] and (2) a pathogen-interaction model that accounts for cross
314 immunity between RSV and human metapneumovirus [20]. Since both models can
315 accurately reproduce the observed epidemic patterns, standard criteria for model
316 validation do not allow us to distinguish between these two models from population-
317 level data alone. Instead, we can measure the empirical resilience of each model
318 by simulating various perturbations and compare them to estimates of empirical re-
319 silience from data, using COVID-19 interventions as an opportunity. Future studies
320 should further investigate using pathogen resilience for validating epidemic models.

321 There are several limitations to our work. First of all, we did not extensively ex-
322 plore other approaches to reconstructing the attractor. Recent studies showed that
323 more sophisticated approaches, such as using non-uniform embedding, can provide
324 more robust reconstruction for noisy data [19]. In the context of causal inference,
325 choices about embedding can have major impact on the resulting inference [25]. Our
326 resilience estimates are likely overly confident given a lack of uncertainties in at-
327 tractr reconstruction as well as the simplicity of our statistical framework. Short
328 pre-pandemic time series also contributes to the crudeness of our estimates. Nonethe-
329 less, as illustrated in our sensitivity analyses (Supplementary Figure S6, S10–S12),
330 inferences about pathogen resilience appear to be robust to decisions about embed-
331 ding lags and dimensions—this is because tracking the rate at which the system
332 approaches the attractor is likely a much simpler problem than making inferences

333 about causal directionality. Our qualitative prediction that common respiratory
334 pathogens are more resilient than prevaccination measles is also likely to be robust
335 to these predictions, given how rapid many respiratory pathogens returned to their
336 original cycles following COVID-19 interventions.

337 Predicting the impact of anthropogenic changes on infectious disease dynamics
338 is a fundamental aim of infectious disease research in a rapidly changing world.
339 Our study illustrates that quantifying pathogen resilience can help us understand
340 how infectious disease pathogens respond to major perturbations caused by public
341 health interventions. More broadly, a detailed understanding of the determinants of
342 pathogen resilience may offer unique insights into pathogen persistence and control-
343 lability.

344 Materials and Methods

345 Data

346 We gathered time series on respiratory infections from four different countries: Canada,
347 Hong Kong, Korea, and United States (US). As a reference, we also included time
348 series data on norovirus infections for available countries—in contrast to respiratory
349 pathogens, we expect gastrointestinal viruses, such as norovirus, to be less affected
350 by COVID-19 intervention measures. For all time series, we rounded every year to
351 52 weeks by taking the average number of cases and tests between the 52nd and
352 53rd week. We also rescale all time series to account for changes in testing patterns,
353 which are then used for the actual analysis.

354 Weekly time series of respiratory infection cases in Canada comes from the Res-
355piratory Virus Detection Surveillance System, which collect data from select lab-
356oratories across Canada. We extract the data from <https://www.canada.ca/en/public-health/services/surveillance/respiratory-virus-detections-canada.html>. To account for an increase in testing from 2013 to 2024, we calculate a 2 year
357 moving average for the number of tests for each pathogen, which we use as a proxy
358 for testing effort. Then, we divide the smoothed testing patterns by the smoothed
359 value at the final week such that the testing effort has a maximum of 1. We then
360 divide weekly cases by the testing effort to obtain a scaled case time series. A similar
361 approach was used earlier for the analysis of RSV time series in the US [22].

362 Weekly time series of respiratory infection cases in Hong Kong comes from the
363 Centre for Health Protection, Department of Health. We extract the data from
364 <https://www.chp.gov.hk/en/statistics/data/10/641/642/2274.html>. We also
365 apply the same scaling procedure to the time series as we did for Canada. For Hong
366 Kong, we only adjust for testing efforts up to the end of 2019 because there was a
367 major reduction in testing for common respiratory pathogens since 2020.

368 Weekly time series of acute respiratory infection cases in Korea comes from Ko-
369 rea Disease Control and Prevention Agency. We extract the data from <https://dportal.kdca.go.kr/pot/is/st/ari.do>. While we do not have information on

373 testing, the reported number of respiratory infections consistently increased from
 374 2013 to the end of 2019, which we interpreted as changes in testing patterns. Since
 375 we do not have testing numbers, we used the weekly sum of all acute respiratory vi-
 376 ral infection cases as a proxy for testing, which were further smoothed with moving
 377 averaged and scaled to have a maximum of 1. For Korea, we also only adjust for
 378 testing efforts up to the end of 2019.

379 Finally, weekly time series of respiratory infection cases in the US comes from
 380 the National Respiratory and Enteric Virus Surveillance System. In the US, there
 381 has been a large increase in testing against some respiratory pathogens, especially
 382 RSV, which could not be corrected for through simple scaling. Instead, we derive an
 383 incidence proxy by multiplying the test positivity with influenza-like illness positivity,
 384 which is taken from <https://gis.cdc.gov/grasp/fluvview/fluportaldashboard.html>.
 385 This method of estimating an incidence proxy has been recently applied in
 386 the analysis of seasonal coronaviruses [26] and Mycoplasma pneumoniae infections
 387 [12]. Detailed assumptions and justifications are provided in [27].

388 **Estimating pathogen resilience**

389 In order to measure pathogen resilience from surveillance data, we first reconstruct
 390 the empirical pre-pandemic attractor of the system using Takens' embedding theorem
 391 [16]. Specifically, for a given pathogen, we take the pre-pandemic (before 2020)
 392 case time series $C(t)$ and reconstruct the attractor using delayed embedding with a
 393 uniform delay of τ and dimension M :

$$X_{\tau,m}(t) = \langle \log(C(t) + 1), \log(C(t - \tau) + 1), \dots, \log(C(t - (M - 1)\tau) + 1) \rangle. \quad (2)$$

394 Here, the delay τ is determined by looking at the autocorrelation of the logged pre-
 395 pandemic time series and asking when the autocorrelation crosses 0 for the first time
 396 [19]; a typical delay for an annual outbreak is around 13 weeks.

397 Then, for a given delay τ , we determine the embedding dimension M using the
 398 false nearest neighbors approach [18, 19]. To do so, we start with an embedding
 399 dimension e and construct a set of points $A_{\tau,e} = \{X_{\tau,e}(t) | t < 2020\}$. Then, for each
 400 point $X_{\tau,e}(t)$, we determine the nearest neighbor from the set $A_{\tau,e}$, which we denote
 401 $X_{\tau,e}(t_{nn})$ for $t \neq t_{nn}$. Then, if the distance between these two points on $e+1$ dimension,
 402 $D_{\tau,e+1}(t) = \|X_{\tau,e+1}(t_{nn}) - X_{\tau,e+1}(t)\|_2$, is larger than their distance on e dimension,
 403 $D_{\tau,e}(t) = \|X_{\tau,e}(t_{nn}) - X_{\tau,e}(t)\|_2$, these two points are deemed to be false nearest
 404 neighbors; specifically, we use a threshold R for the ratio between two distances
 405 $D_{\tau,e+1}(t)/D_{\tau,e}(t)$ to determine false nearest neighbors. In the main text, we determine
 406 embedding dimension based as the first dimension without any false nearest neighbors
 407 for $R = 10$. In Supplementary Materials, we impose $R = 5$ to select for higher
 408 dimensions. Once we determine the embedding lag τ and dimension M , we apply
 409 the embedding to the entire time series and calculate the nearest neighbor distance
 410 against the attractor $A_{\tau,M}$ to obtain a time series of distance from attractor $D_{\tau,M}(t)$.

411 From a time series of distance from attractor, we estimate pathogen resilience
 412 by fitting a linear regression to an appropriate window. To automatically select
 413 the fitting window, we begin by smoothing the distance time series using locally
 414 estimated scatterplot smoothing (LOESS) to obtain $\hat{D}_{\tau,M}(t)$, where the smoothing
 415 is performed on a log scale and exponentiated afterwards. Then, we determine
 416 threshold values (T_{start} and T_{end}) for the smoothed distances and choose the fitting
 417 window based on when $\hat{D}_{\tau,M}(t)$ crosses these threshold values for the first time.
 418 These thresholds are determined by first calculating maximum distance,

$$\max \hat{D} = \max \hat{D}_{\tau,M}(t), \quad (3)$$

419 and mean pre-pandemic distance,

$$\hat{D}_{\text{mean}} = \frac{1}{N_{t < 2020}} \sum_{t < 2020} \hat{D}_{\tau,M}(t), \quad (4)$$

420 as a reference, and then dividing their ratios into 10 equal bins:

$$T_{\text{start}} = \hat{D}_{\text{mean}} \times \left(\frac{\max \hat{D}}{\hat{D}_{\text{mean}}} \right)^{9/10} \quad (5)$$

$$T_{\text{end}} = \hat{D}_{\text{mean}} \times \left(\frac{\max \hat{D}}{\hat{D}_{\text{mean}}} \right)^{1/10} \quad (6)$$

421 This allows us to discard the initial period during which the distance increases (from
 422 the introduction of intervention measures) and the final period during which the
 423 distance plateaus (as the system reaches an attractor). The fitting window is deter-
 424 mined based on when the smoothed distance $\hat{D}_{\tau,M}(t)$ crosses these threshold values
 425 for the first time; then, we fit a linear regression to logged (unsmoothed) distances
 426 $\log D_{\tau,M}(t)$ using that window.

427 Mathematical modeling

428 Throughout the paper, we use a series of mathematical models to illustrate the con-
 429 cept of pathogen resilience and to understand the determinants of pathogen resilience.
 430 In general, the intrinsic resilience for a given system is given by the largest real part
 431 of the eigenvalues of the linearized system at endemic equilibrium. Here, we focus on
 432 the SIRS model and present the details of other models in Supplementary Materials.
 433 The SIRS (Susceptible-Infected-Recovered-Susceptible) model is the simplest model
 434 that allows for waning of immunity, where recovered (immune) individuals are as-
 435 sumed to become fully susceptible after an average of $1/\delta$ time period. The dynamics
 436 of the SIRS model is described by the following set of differential equations:

$$\frac{dS}{dt} = \mu - \beta(t)SI - \mu S + \delta R \quad (7)$$

$$\frac{dI}{dt} = \beta(t)SI - (\gamma + \mu)I \quad (8)$$

$$\frac{dR}{dt} = \gamma I - (\delta + \mu)R \quad (9)$$

(10)

437 where μ represents the birth/death rate, $\beta(t)$ represents the time-varying trans-
 438 mission rate, and γ represents the recovery rate. The basic reproduction number
 439 $\mathcal{R}_0 = \beta(t)/(\gamma + \mu)$ is defined as the average number of secondary infections caused
 440 by a single infected individual in a fully susceptible population and measures the
 441 intrinsic transmissibility of a pathogen.

442 When we first introduce the idea of pathogen resilience (Figure 2), we impose
 443 sinusoidal changes to the transmission rate to account for seasonal transmission:

$$\beta(t) = b_1(1 + \theta \cos(2\pi(t - \phi)))\alpha(t), \quad (11)$$

444 where b_1 represents the baseline transmission rate, θ represents the seasonal ampli-
 445 tude, and ϕ represents the seasonal offset term. Here, we also introduce an extra
 446 multiplicative term $\alpha(t)$ to account for the impact of COVID-19 interventions, where
 447 $\alpha(t) < 1$ indicates transmission reduction. Figure 2A and 2B are generated assuming
 448 $b_1 = 3 \times (365/7 + 1/50)/\text{years}$, $\theta = 0.2$, $\phi = 0$, $\mu = 1/50/\text{years}$, $\gamma = 365/7/\text{years}$, and
 449 $\delta = 1/2/\text{years}$. In Figure 2A, we impose a 50% transmission reduction for 6 months
 450 from 2020:

$$\alpha(t) = \begin{cases} 0.5 & 2020 \leq t < 2020.5 \\ 1 & \text{otherwise} \end{cases} \quad (12)$$

451 In Figure 2B, we impose a 50% transmission reduction for 6 months from 2020 and
 452 a permanent 10% reduction onward:

$$\alpha(t) = \begin{cases} 1 & t < 2020 \\ 0.5 & 2020 \leq t < 2020.5 \\ 0.9 & 2020.5 \leq t \end{cases} \quad (13)$$

453 In both scenarios, we simulate the SIRS model from the following initial conditions
 454 ($S(0) = 1/\mathcal{R}_0$, $I(0) = 1 \times 10^{-6}$, and $R(0) = 1 - S(0) - I(0)$) from 1900 until 2030.

455 To measure the empirical resilience of the SIR model (Figure 2C and 2F), we
 456 compute the normalized distance between post-intervention susceptible and logged
 457 infected proportions and their corresponding pre-intervention values at the same time
 458 of year:

$$\sqrt{\left(\frac{S(t) - S_{\text{pre}}(t)}{\sigma_S}\right)^2 + \left(\frac{\log I(t) - \log I_{\text{pre}}(t)}{\sigma_{\log I}}\right)^2}, \quad (14)$$

459 where σ_S and $\sigma_{\log I}$ represent the standard deviation in the pre-intervention suscep-
 460 tible and logged infected proportions. We normalize the differences in susceptible
 461 and logged infected proportions to allow both quantities to equally contribute to the

⁴⁶² changes in distance from attractor. In Supplementary Materials, we also compare
⁴⁶³ the how the degree of seasonal transmission affects empirical resilience by varying
⁴⁶⁴ θ from 0 to 0.4; when we assume no seasonality ($\theta = 0$), we do not normalize the
⁴⁶⁵ distance because the standard deviation of pre-intervention dynamics are zero.

⁴⁶⁶ Finally, we use the SIRS model to understand how underlying epidemiological
⁴⁶⁷ parameters affect pathogen resilience and link this relationship to underlying sus-
⁴⁶⁸ ceptible host dynamics. For the simple SIRS model without seasonal transmission
⁴⁶⁹ ($\theta = 0$), the intrinsic resilience corresponds to:

$$-\frac{\text{Re}(\lambda)}{2} = \frac{\delta + \beta I^* + \mu}{2}. \quad (15)$$

⁴⁷⁰ Here, I^* represents the prevalence values at endemic equilibrium:

$$I^* = \frac{(\delta + \mu)(\beta - (\gamma + \mu))}{\beta(\delta + \gamma + \mu)}. \quad (16)$$

⁴⁷¹ The susceptible replenishment rate is given by:

$$S_{\text{replenish}} = \frac{\mu + \delta R}{S^*}, \quad (17)$$

⁴⁷² where $S^* = 1/\mathcal{R}_0$ represents the equilibrium proportion of susceptible individuals.
⁴⁷³ We vary the basic reproduction number \mathcal{R}_0 between 1.1 to 6 and the average duration
⁴⁷⁴ of immunity $1/\delta$ between 2 to 80 years, and compute these two quantities. In doing
⁴⁷⁵ so, we fix all other parameters: $\mu = 1/80/\text{years}$ and $\gamma = 365/7/\text{years}$.

⁴⁷⁶ **Supplementary Text**

⁴⁷⁷ **Resilience of a stage-structured system.**

⁴⁷⁸ In Figure 2G–I, we use a more realistic, stage-structured model to illustrate how
⁴⁷⁹ transient phenomena can cause the system to slow down. Specifically, we use the
⁴⁸⁰ stage-structured RSV model proposed by [22], which assumes that subsequent rein-
⁴⁸¹ fections cause an individual to become less susceptible and transmissible than previ-
⁴⁸² ous infections. The model dynamics can be described as follows:

$$\frac{dM}{dt} = \mu - (\omega + \mu)M \quad (S1)$$

$$\frac{dS_0}{dt} = \omega M - (\lambda(t) + \mu)S_0 \quad (S2)$$

$$\frac{dI_1}{dt} = \lambda(t)S_0 - (\gamma_1 + \mu)I_1 \quad (S3)$$

$$\frac{dS_1}{dt} = \gamma_1 I_1 - (\sigma_1 \lambda(t) + \mu)S_1 \quad (S4)$$

$$\frac{dI_2}{dt} = \sigma_1 \lambda(t)S_1 - (\gamma_2 + \mu)I_2 \quad (S5)$$

$$\frac{dS_2}{dt} = \gamma_2 I_2 - (\sigma_2 \lambda(t) + \mu)S_2 \quad (S6)$$

$$\frac{dI_3}{dt} = \sigma_2 \lambda(t)S_2 - (\gamma_3 + \mu)I_3 \quad (S7)$$

$$\frac{dS_3}{dt} = \gamma_3 I_3 - (\sigma_3 \lambda(t) + \mu)S_3 + \gamma_4 I_4 \quad (S8)$$

$$\frac{dI_4}{dt} = \sigma_3 \lambda(t)S_3 - (\gamma_4 + \mu)I_4 \quad (S9)$$

$$(S10)$$

⁴⁸³ where M represents the proportion of individuals who are maternally immune; S_i
⁴⁸⁴ represents the proportion of individuals who are susceptible after i prior infections; I_i
⁴⁸⁵ represents the proportion of individuals who are currently (re)-infected with their i -th
⁴⁸⁶ infection; μ represents the birth and death rates; $1/\omega$ represents the mean duration
⁴⁸⁷ of maternal immunity; $1/\gamma_i$ represents the mean duration of infection; $\lambda(t)$ represents
⁴⁸⁸ the force of infection; and σ_i represents the reduction in susceptibility for reinfection.
⁴⁸⁹ The force of infection is modeled using a sinusoidal function:

$$\beta(t) = b_1(1 + \theta \cos(2\pi(t - \phi)))\alpha(t) \quad (S11)$$

$$\lambda(t) = \beta(I_1 + \rho_1 I_2 + \rho_2(I_3 + I_4)), \quad (S12)$$

⁴⁹⁰ where b_1 represents the baseline transmission rate; θ represents the seasonal ampli-
⁴⁹¹ tude; ϕ represents the seasonal offset term; $\alpha(t)$ represents the intervention effect;
⁴⁹² and ρ_i represents the impact of immunity on transmission reduction. We use the

⁴⁹³ following parameters to simulate the impact of interventions on epidemic dynam-
⁴⁹⁴ ics [22]: $b_1 = 9 \times (365/10 + 1/80)/\text{years}$, $\theta = 0.2$, $\phi = -0.1$, $\omega = 365/112/\text{years}$,
⁴⁹⁵ $\gamma_1 = 365/10/\text{years}$, $\gamma_2 = 365/7/\text{years}$, $\gamma_3 = 365/5/\text{years}$, $\sigma_1 = 0.76$, $\sigma_2 = 0.6$,
⁴⁹⁶ $\sigma_3 = 0.4$, $\rho_1 = 0.75$, $\rho_2 = 0.51$, and $\mu = 1/80/\text{years}$. We assume a 50% transmission
⁴⁹⁷ reduction for 6 months from 2020:

$$\alpha(t) = \begin{cases} 0.5 & 2020 \leq t < 2020.5 \\ 1 & \text{otherwise} \end{cases} \quad (\text{S13})$$

⁴⁹⁸ The model is simulated from 1900 to 2030 using the following initial conditions:
⁴⁹⁹ $M = 0$, $S_0 = 1/\mathcal{R}_0 - I_1$, $I_1 = 1 \times 10^{-6}$, $S_1 = 1 - 1/\mathcal{R}_0$, $I_2 = 0$, $S_2 = 0$, $I_3 = 0$,
⁵⁰⁰ $S_3 = 0$, and $I_4 = 0$. For the phase plane analysis (Figure 2H) and distance analysisus
⁵⁰¹ (Figure 2I), we rely on the average susceptibility,

$$\bar{S} = S_0 + \sigma_1 S_1 + \sigma_2 S_2 + \sigma_3 S_3, \quad (\text{S14})$$

⁵⁰² and total prevalence,

$$I_{\text{total}} = I_1 + I_2 + I_3 + I_4. \quad (\text{S15})$$

⁵⁰³ These quantities are used to compute the normalized distance from the attractor, as
⁵⁰⁴ described in the main text.

⁵⁰⁵ Resilience of a multistain system.

⁵⁰⁶ We use a simple two-strain model to show that a multistain host-pathogen system
⁵⁰⁷ that is coupled through cross immunity can be described by a single resilience value.
⁵⁰⁸ The model dynamics can be described as follows [20]:

$$\frac{dS}{dt} = \mu - \mu S - (\lambda_1 + \lambda_2)S + \rho_1 R_1 + \rho_2 R_2 \quad (\text{S16})$$

$$\frac{dI_1}{dt} = \lambda_1 S - (\gamma_1 + \mu)I_1 \quad (\text{S17})$$

$$\frac{dI_2}{dt} = \lambda_2 S - (\gamma_2 + \mu)I_2 \quad (\text{S18})$$

$$\frac{dR_1}{dt} = \gamma_1 I_1 - \lambda_2 \epsilon_{21} R_1 - \rho_1 R_1 + \rho_2 R - \mu R_1 \quad (\text{S19})$$

$$\frac{dR_2}{dt} = \gamma_2 I_2 - \lambda_1 \epsilon_{12} R_2 - \rho_2 R_2 + \rho_1 R - \mu R_2 \quad (\text{S20})$$

$$\frac{dJ_1}{dt} = \lambda_1 \epsilon_{12} R_2 - (\gamma_1 + \mu) J_1 \quad (\text{S21})$$

$$\frac{dJ_2}{dt} = \lambda_2 \epsilon_{21} R_1 - (\gamma_2 + \mu) J_2 \quad (\text{S22})$$

$$\frac{dR}{dt} = \gamma_1 J_1 + \gamma_2 J_2 - \rho_1 R - \rho_2 R - \mu R \quad (\text{S23})$$

where S represents the proportion of individuals who are fully susceptible to infections by both strains; I_1 represents the proportion of individuals who are infected with strain 1 without prior immunity; I_2 represents the proportion of individuals who are infected with strain 2 without prior immunity; R_1 represents the proportion of individuals who are fully immune against strain 1 and partially susceptible to reinfection by strain 2; R_2 represents the proportion of individuals who are fully immune against strain 2 and partially susceptible to reinfection by strain 1; J_1 represents the proportion of individuals who are infected with strain 1 with prior immunity against strain 2; J_2 represents the proportion of individuals who are infected with strain 2 with prior immunity against strain 1; R represents the proportion of individuals who are immune to infections from both strains; μ represents the birth/death rate; λ_1 and λ_2 represent the force of infection from strains 1 and 2, respectively; ρ_1 and ρ_2 represent the waning immunity rate; γ_1 and γ_2 represent the recovery rate; ϵ_{12} and ϵ_{21} represent the susceptibility to reinfection with strains 2 and 1, respectively, given prior immunity from infection with strains 1 and 2, respectively. The force of infection is modeled as follows:

$$\beta_1 = b_1(1 + \theta_1 \sin(2\pi(t - \phi_1)))\alpha(t) \quad (\text{S24})$$

$$\beta_2 = b_2(1 + \theta_2 \sin(2\pi(t - \phi_2)))\alpha(t) \quad (\text{S25})$$

$$\lambda_1 = \beta_1(I_1 + J_1) \quad (\text{S26})$$

$$\lambda_2 = \beta_2(I_2 + J_2) \quad (\text{S27})$$

In Supplementary Figures S2–S4, we assume the following parameters: $b_1 = 2 \times 52/\text{years}$, $b_2 = 4 \times 52/\text{years}$, $\phi_1 = \phi_2 = 0$, $\epsilon_{12} = 0.9$, $\epsilon_{21} = 0.5$, $\gamma_1 = \gamma_2 = 52/\text{years}$, $\rho_1 = \rho_2 = 1/\text{years}$, and $\mu = 1/70/\text{years}$. For all simulations, we assume a 50% transmission reduction for 6 months from 2020:

$$\alpha(t) = \begin{cases} 0.5 & 2020 \leq t < 2020.5 \\ 1 & \text{otherwise} \end{cases} \quad (\text{S28})$$

The seasonal amplitude θ is varied from 0 to 0.4. All simulations are ran from 1900 to 2030 from the following initial conditions: $S(0) = 1 - 2 \times 10^{-6}$, $I_1(0) = 1 \times 10^{-6}$, $I_2(0) = 1 \times 10^{-6}$, $R_1(0) = 0$, $R_2(0) = 0$, $J_1(0) = 0$, $J_2(0) = 0$, and $R(0) = 0$.

For this, we consider three different scenarios for measuring pathogen resilience: (1) we only have information about strain 1, (2) we only have information about strain 2, and (3) we are unable to distinguish the differences between strains. In the first two scenarios (see panels A–C for strain 1 and panels D–F for strain 2), we consider the dynamics of average susceptibility for each strain and total prevalence:

$$\bar{S}_1 = S + \epsilon_{12}R_2 \quad (\text{S29})$$

$$\hat{I}_1 = I_1 + J_1 \quad (\text{S30})$$

$$\bar{S}_2 = S + \epsilon_{21}R_1 \quad (\text{S31})$$

$$\hat{I}_2 = I_2 + J_2 \quad (\text{S32})$$

⁵³⁷ In the third scenario (panels G–I), we consider the dynamics of total susceptible
⁵³⁸ and infected population:

$$\hat{S} = S + R_2 + R_1 \quad (\text{S33})$$

$$\hat{I} = I_1 + J_1 + I_2 + J_2 \quad (\text{S34})$$

$$(\text{S35})$$

⁵³⁹ These quantities are used to compute the normalized distance from the attractor, as
⁵⁴⁰ described in the main text.

⁵⁴¹ Estimating intrinsic resilience using mechanistic model

⁵⁴² We test whether we can reliably estimate the intrinsic resilience of a system by fitting
⁵⁴³ a mechanistic model. Specifically, we simulate case time series from stochastic SIRS
⁵⁴⁴ and two-strain models and fit a simple, deterministic SIRS model using a Bayesian
⁵⁴⁵ framework.

⁵⁴⁶ First, we describe the simulation set up. The stochastic SIRS model can be
⁵⁴⁷ written as follows:

$$\beta(t) = \mathcal{R}_0 \left(1 + \theta \cos \left(\frac{2\pi t}{364} \right) \right) \alpha(t)(1 - \exp(-\gamma)) \quad (\text{S36})$$

$$\text{FOI}(t) = \beta(t)I(t - \Delta t)/N \quad (\text{S37})$$

$$B(t) \sim \text{Poisson}(\mu N) \quad (\text{S38})$$

$$\Delta S(t) \sim \text{Binom}(S(t - \Delta t), 1 - \exp(-(\text{FOI}(t) + \mu)\Delta t)) \quad (\text{S39})$$

$$N_{SI}(t) \sim \text{Binom}\left(\Delta S(t), \frac{\text{FOI}(t)}{\text{FOI}(t) + \mu}\right) \quad (\text{S40})$$

$$\Delta I(t) \sim \text{Binom}(I(t - \Delta t), 1 - \exp(-(\gamma + \mu)\Delta t)) \quad (\text{S41})$$

$$N_{IR}(t) \sim \text{Binom}\left(\Delta I(t), \frac{\gamma}{\gamma + \mu}\right) \quad (\text{S42})$$

$$\Delta R(t) \sim \text{Binom}(R(t - \Delta t), 1 - \exp(-(\delta + \mu)\Delta t)) \quad (\text{S43})$$

$$N_{RS}(t) \sim \text{Binom}\left(\Delta R(t), \frac{\delta}{\delta + \mu}\right) \quad (\text{S44})$$

$$S(t) = S(t - \Delta t) + N_{RS}(t) + B(t) - \Delta S(t) \quad (\text{S45})$$

$$I(t) = I(t - \Delta t) + N_{SI}(t) - \Delta I(t) \quad (\text{S46})$$

$$R(t) = R(t - \Delta t) + N_{IR}(t) - \Delta R(t) \quad (\text{S47})$$

⁵⁴⁸ where FOI represent the force of infection; N_{ij} represent the number of individuals
⁵⁴⁹ moving from compartment i to j on a given day; and $B(t)$ represents the number
⁵⁵⁰ of new births. We simulate the model on a daily scale—assuming 364 days in a
⁵⁵¹ year so that it can be evenly grouped into 52 weeks—with the following parameters:
⁵⁵² $\mathcal{R}_0 = 3$, $\theta = 0.1$, $\gamma = 1/7/\text{days}$, $\delta = 1/(364 \times 2)/\text{days}$, $\mu = 1/(364 \times 50)/\text{days}$, and

⁵⁵³ $N = 1 \times 10^8$. The model is simulated from 1900 to 2030 assuming $S(0) = N/3$,
⁵⁵⁴ $I(0) = 100$, and $R(0) = N - S(0) - I(0)$. The observed incidence from the model is
⁵⁵⁵ then simulated as follows:

$$C(t) = \text{Beta} - \text{Binom}(N_{SI}(t), \rho, k), \quad (\text{S48})$$

⁵⁵⁶ where ρ represents the reporting probability and k represents the overdispersion pa-
⁵⁵⁷ rameter of beta-binomial distribution. We assume $\rho = 0.002$ (i.e., 0.2% probability)
⁵⁵⁸ and $k = 1000$.

⁵⁵⁹ The stochastic two-strain model can be written as follows:

$$\beta_1(t) = b_1 (1 + \theta_1 \cos(2\pi(t - \phi_1))) \alpha(t) \quad (\text{S49})$$

$$\beta_2(t) = b_2 (1 + \theta_2 \cos(2\pi(t - \phi_2))) \alpha(t) \quad (\text{S50})$$

$$\text{FOI}_1(t) = \beta_1(t)(I_1(t - \Delta t) + J_1(t - \Delta t))/N \quad (\text{S51})$$

$$\text{FOI}_2(t) = \beta_2(t)(I_2(t - \Delta t) + J_2(t - \Delta t))/N \quad (\text{S52})$$

$$B(t) \sim \text{Poisson}(\mu N) \quad (\text{S53})$$

$$\Delta S(t) \sim \text{Binom}(S(t - \Delta t), 1 - \exp(-(\text{FOI}_1(t) + \text{FOI}_2(t) + \mu)\Delta t)) \quad (\text{S54})$$

$$N_{SI_1}(t) \sim \text{Binom}\left(\Delta S(t), \frac{\text{FOI}_1(t)}{\text{FOI}_1(t) + \text{FOI}_2(t) + \mu}\right) \quad (\text{S55})$$

$$N_{SI_2}(t) \sim \text{Binom}\left(\Delta S(t), \frac{\text{FOI}_2(t)}{\text{FOI}_1(t) + \text{FOI}_2(t) + \mu}\right) \quad (\text{S56})$$

$$\Delta I_1(t) \sim \text{Binom}(I_1(t - \Delta t), 1 - \exp(-(\gamma_1 + \mu)\Delta t)) \quad (\text{S57})$$

$$N_{I_1 R_1}(t) \sim \text{Binom}\left(\Delta I_1(t), \frac{\gamma_1}{\gamma_1 + \mu}\right) \quad (\text{S58})$$

$$\Delta I_2(t) \sim \text{Binom}(I_2(t - \Delta t), 1 - \exp(-(\gamma_2 + \mu)\Delta t)) \quad (\text{S59})$$

$$N_{I_2 R_2}(t) \sim \text{Binom}\left(\Delta I_2(t), \frac{\gamma_2}{\gamma_2 + \mu}\right) \quad (\text{S60})$$

$$\Delta R_1(t) \sim \text{Binom}(R_1(t - \Delta t), 1 - \exp(-(\epsilon_{21}\text{FOI}_2(t) + \rho_1 + \mu)\Delta t)) \quad (\text{S61})$$

$$N_{R_1 S}(t) \sim \text{Binom}\left(\Delta R_1(t), \frac{\rho_1}{\epsilon_{21}\text{FOI}_2(t) + \rho_1 + \mu}\right) \quad (\text{S62})$$

$$N_{R_1 J_2}(t) \sim \text{Binom}\left(\Delta R_1(t), \frac{\epsilon_{21}\text{FOI}_2(t)}{\epsilon_{21}\text{FOI}_2(t) + \rho_1 + \mu}\right) \quad (\text{S63})$$

$$\Delta R_2(t) \sim \text{Binom}(R_2(t - \Delta t), 1 - \exp(-(\epsilon_{12}\text{FOI}_1(t) + \rho_2 + \mu)\Delta t)) \quad (\text{S64})$$

$$N_{R_2 S}(t) \sim \text{Binom}\left(\Delta R_2(t), \frac{\rho_2}{\epsilon_{12}\text{FOI}_1(t) + \rho_2 + \mu}\right) \quad (\text{S65})$$

$$N_{R_2 J_1}(t) \sim \text{Binom}\left(\Delta R_2(t), \frac{\epsilon_{12}\text{FOI}_1(t)}{\epsilon_{12}\text{FOI}_1(t) + \rho_2 + \mu}\right) \quad (\text{S66})$$

$$\Delta J_1(t) \sim \text{Binom}(J_1(t - \Delta t), 1 - \exp(-(\gamma_1 + \mu)\Delta t)) \quad (\text{S67})$$

$$N_{J_1 R}(t) \sim \text{Binom}\left(\Delta J_1(t), \frac{\gamma_1}{\gamma_1 + \mu}\right) \quad (\text{S68})$$

$$\Delta J_2(t) \sim \text{Binom}(J_2(t - \Delta t), 1 - \exp(-(\gamma_2 + \mu)\Delta t)) \quad (\text{S69})$$

$$N_{J_2R}(t) \sim \text{Binom}\left(\Delta J_2(t), \frac{\gamma_2}{\gamma_2 + \mu}\right) \quad (\text{S70})$$

$$\Delta R(t) \sim \text{Binom}(R(t - \Delta t), 1 - \exp(-(\rho_1 + \rho_2 + \mu)\Delta t)) \quad (\text{S71})$$

$$N_{RR_1}(t) \sim \text{Binom}\left(\Delta R(t), \frac{\rho_1}{\rho_1 + \rho_2 + \mu}\right) \quad (\text{S72})$$

$$N_{RR_2}(t) \sim \text{Binom}\left(\Delta R(t), \frac{\rho_2}{\rho_1 + \rho_2 + \mu}\right) \quad (\text{S73})$$

$$S(t) = S(t - \Delta t) - \Delta S(t) + B(t) + N_{R_1S}(t) + N_{R_2S}(t) \quad (\text{S74})$$

$$I_1(t) = I_1(t - \Delta t) - \Delta I_1(t) + N_{SI_1}(t) \quad (\text{S75})$$

$$I_2(t) = I_2(t - \Delta t) - \Delta I_2(t) + N_{SI_2}(t) \quad (\text{S76})$$

$$R_1(t) = R_1(t - \Delta t) - \Delta R_1(t) + N_{I_1R_1}(t) + N_{RR_1}(t) \quad (\text{S77})$$

$$R_2(t) = R_2(t - \Delta t) - \Delta R_2(t) + N_{I_2R_2}(t) + N_{RR_2}(t) \quad (\text{S78})$$

$$J_1(t) = J_1(t - \Delta t) - \Delta J_1(t) + N_{R_2J_1}(t) \quad (\text{S79})$$

$$J_2(t) = J_2(t - \Delta t) - \Delta J_2(t) + N_{R_1J_2}(t) \quad (\text{S80})$$

$$R(t) = R(t - \Delta t) - \Delta R(t) + N_{J_1R}(t) + N_{J_2R}(t) \quad (\text{S81})$$

Supplementary Figures

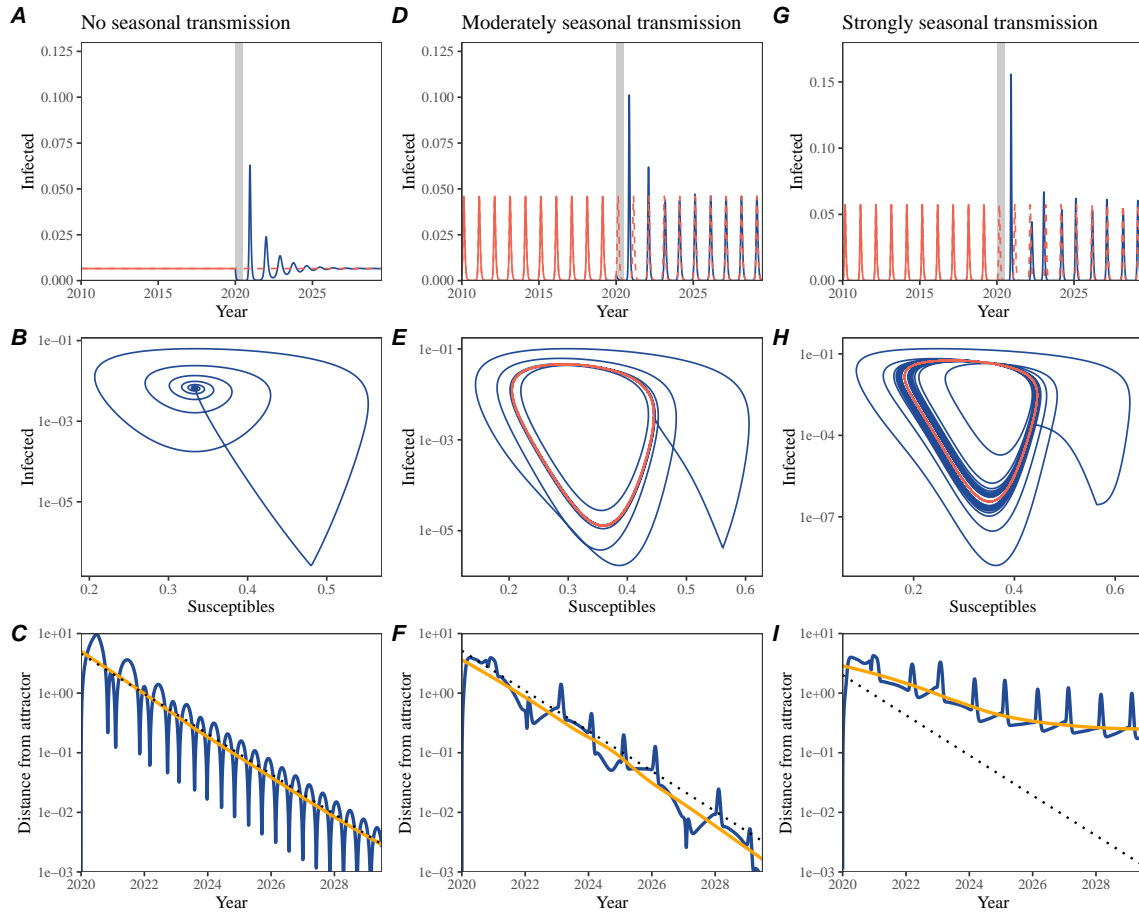


Figure S1: Impact of seasonal transmission on pathogen resilience. (A, D, G) Simulated epidemic trajectories using the SIRS model without seasonal forcing (A), with seasonal forcing of amplitude of 0.2 (D), and with seasonal forcing of amplitude of 0.2 (G). Red and blue solid lines represent epidemic dynamics before and after interventions are introduced, respectively. Red dashed lines represent counterfactual epidemic dynamics in the absence of interventions. Gray regions indicate the duration of interventions. (B, E, H) Phase plane representation of the corresponding model. Red and blue solid lines represent epidemic trajectories on an SI phase plane before and after interventions are introduced, respectively. (C, F, I) Changes in logged distance from attractor over time. Blue lines represent the logged distance from attractor. Orange lines represent the locally estimated scatterplot smoothing (LOESS) fits to the logged distance from attractor. Dotted lines are superimposed as a comparison to have the same slope as the intrinsic resilience of the seasonally unforced system.

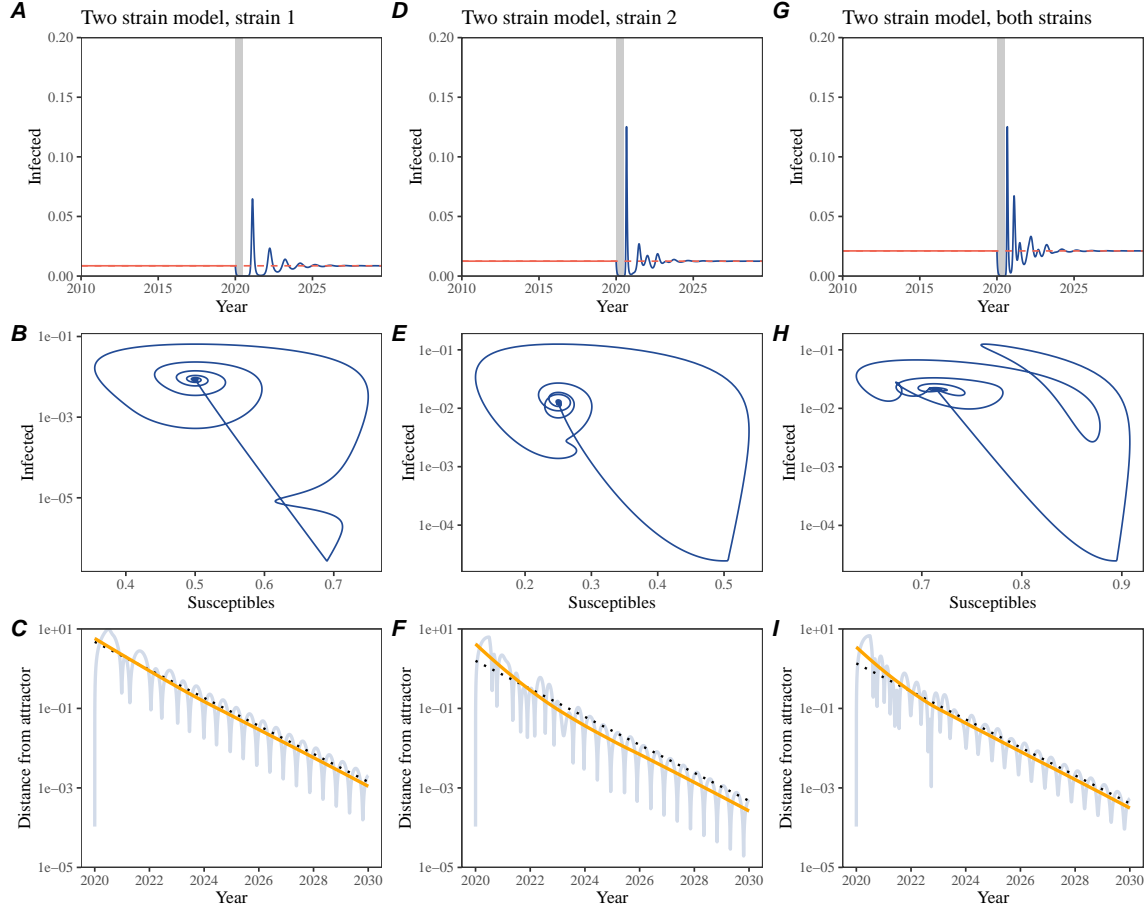


Figure S2: Conceptual framework for measuring pathogen resilience following NPIs for a multi-strain system without seasonal forcing. (A, D, G) Simulated epidemic trajectories using a multi-strain system without seasonal forcing. Red and blue solid lines represent epidemic dynamics before and after interventions are introduced, respectively. Red dashed lines represent counterfactual epidemic dynamics in the absence of interventions. Gray regions indicate the duration of interventions. (B, E, H) Phase plane representation of the corresponding model. Red and blue solid lines represent epidemic trajectories on an SI phase plane before and after interventions are introduced, respectively. (C, F, I) Changes in logged distance from attractor over time. Blue lines represent the logged distance from attractor. Orange lines represent the locally estimated scatterplot smoothing (LOESS) fits to the logged distance from attractor. Dotted lines are superimposed as a comparison to have the same slope as the intrinsic resilience of the seasonally unforced system.

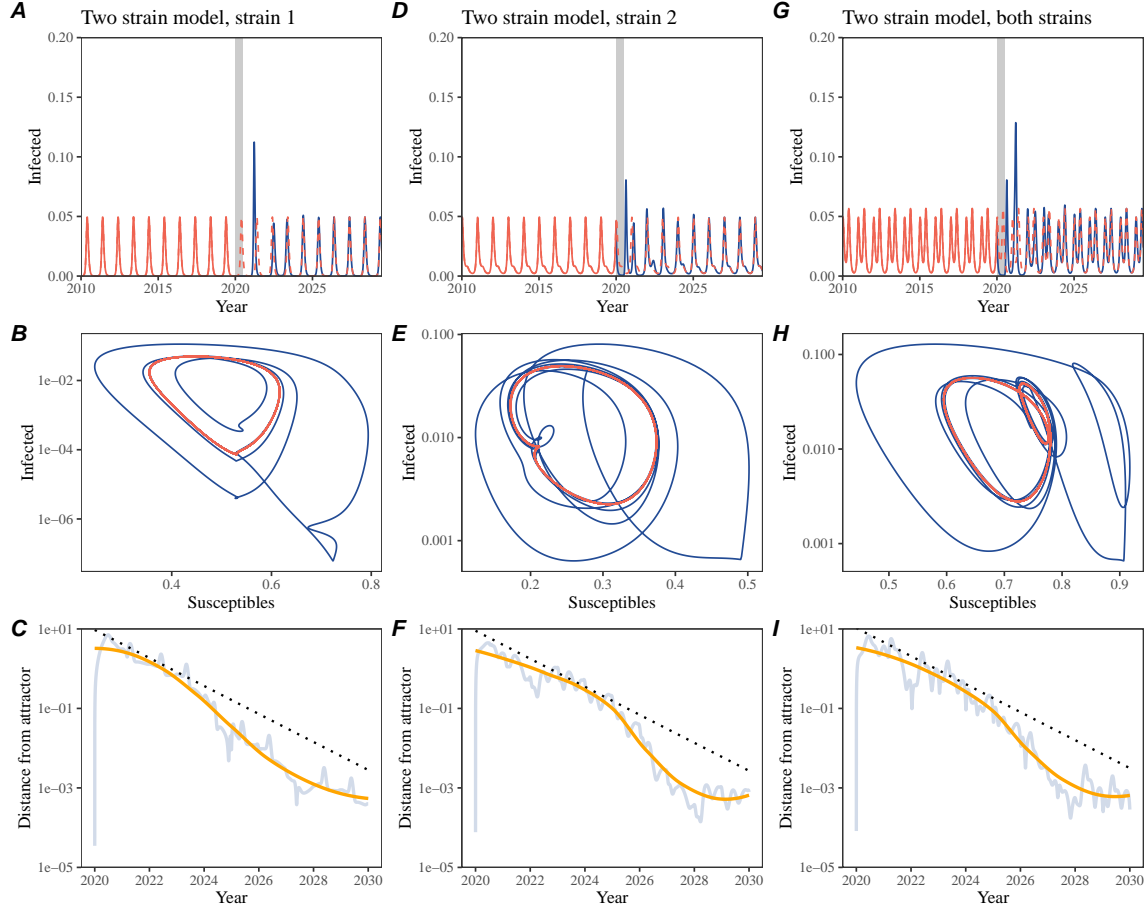


Figure S3: Conceptual framework for measuring pathogen resilience following NPIs for a multi-strain system with seasonal forcing. (A, D, G) Simulated epidemic trajectories using a multi-strain system with seasonal forcing (amplitude of 0.2). Red and blue solid lines represent epidemic dynamics before and after interventions are introduced, respectively. Red dashed lines represent counterfactual epidemic dynamics in the absence of interventions. Gray regions indicate the duration of interventions. (B, E, H) Phase plane representation of the corresponding model. Red and blue solid lines represent epidemic trajectories on an SI phase plane before and after interventions are introduced, respectively. (C, F, I) Changes in logged distance from attractor over time. Blue lines represent the logged distance from attractor. Orange lines represent the locally estimated scatterplot smoothing (LOESS) fits to the logged distance from attractor. Dotted lines are superimposed as a comparison to have the same slope as the intrinsic resilience of the seasonally unforced system.

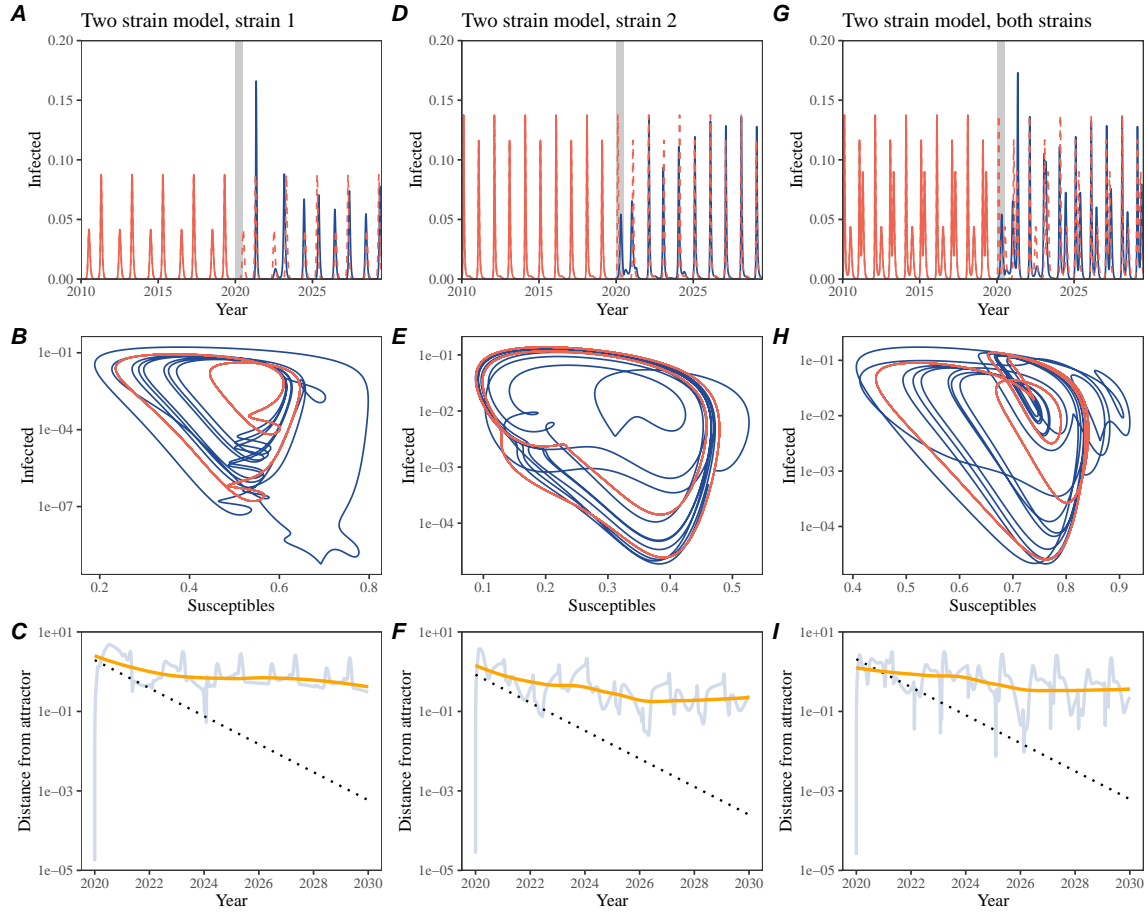


Figure S4: Conceptual framework for measuring pathogen resilience following NPIs for a multi-strain system with strong seasonal forcing. (A, D, G) Simulated epidemic trajectories using a multi-strain system with seasonal forcing (amplitude of 0.4). Red and blue solid lines represent epidemic dynamics before and after interventions are introduced, respectively. Red dashed lines represent counterfactual epidemic dynamics in the absence of interventions. Gray regions indicate the duration of interventions. (B, E, H) Phase plane representation of the corresponding model. Red and blue solid lines represent epidemic trajectories on an SI phase plane before and after interventions are introduced, respectively. (C, F, I) Changes in logged distance from attractor over time. Blue lines represent the logged distance from attractor. Orange lines represent the locally estimated scatterplot smoothing (LOESS) fits to the logged distance from attractor. Dotted lines are superimposed as a comparison to have the same slope as the intrinsic resilience of the seasonally unforced system.

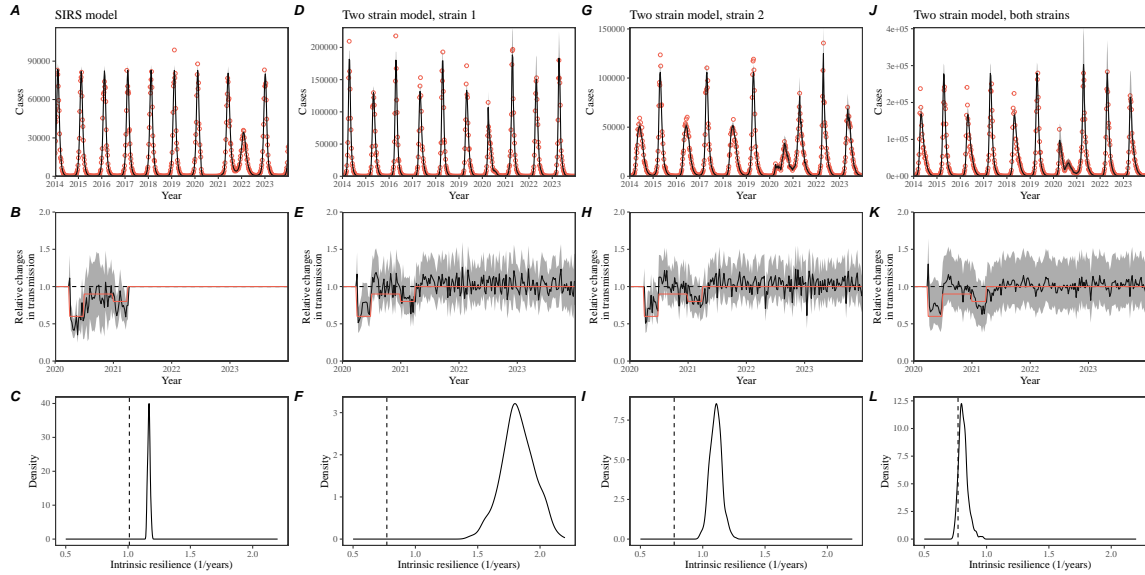


Figure S5: Mechanistic model fits to simulated data and inferred intrinsic resilience. (A, D, G, J) Simulated case time series from corresponding models (red) and SIRS model fits (black). (B, E, H, K) Assumed changes in transmission due to COVID-19 interventions (red) and estimated changes from the SIRS model (black). Solid lines and shaded regions represent fitted posterior median and 95% credible intervals. (C, F, I, L) True intrinsic resilience of the seasonally unforced system (vertical lines) and the posterior distribution of the inferred intrinsic resilience from the SIRS model (density plots).

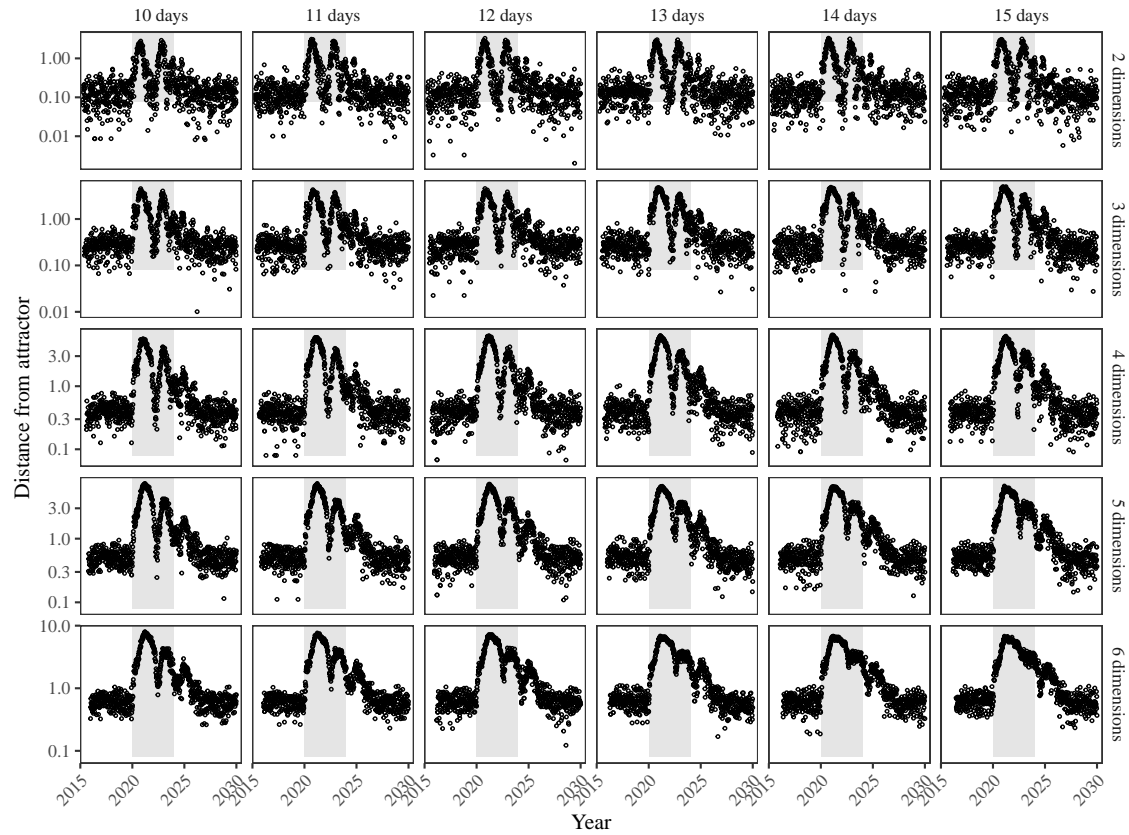


Figure S6: Sensitivity of the distance from attractor to choices about embedding lags and dimensions. Sensitivity analysis for the distance-from-attractor time series shown in Figure 3E in the main text by varying the embedding lag between 10–15 days and embedding dimensions between 2–6 dimensions.

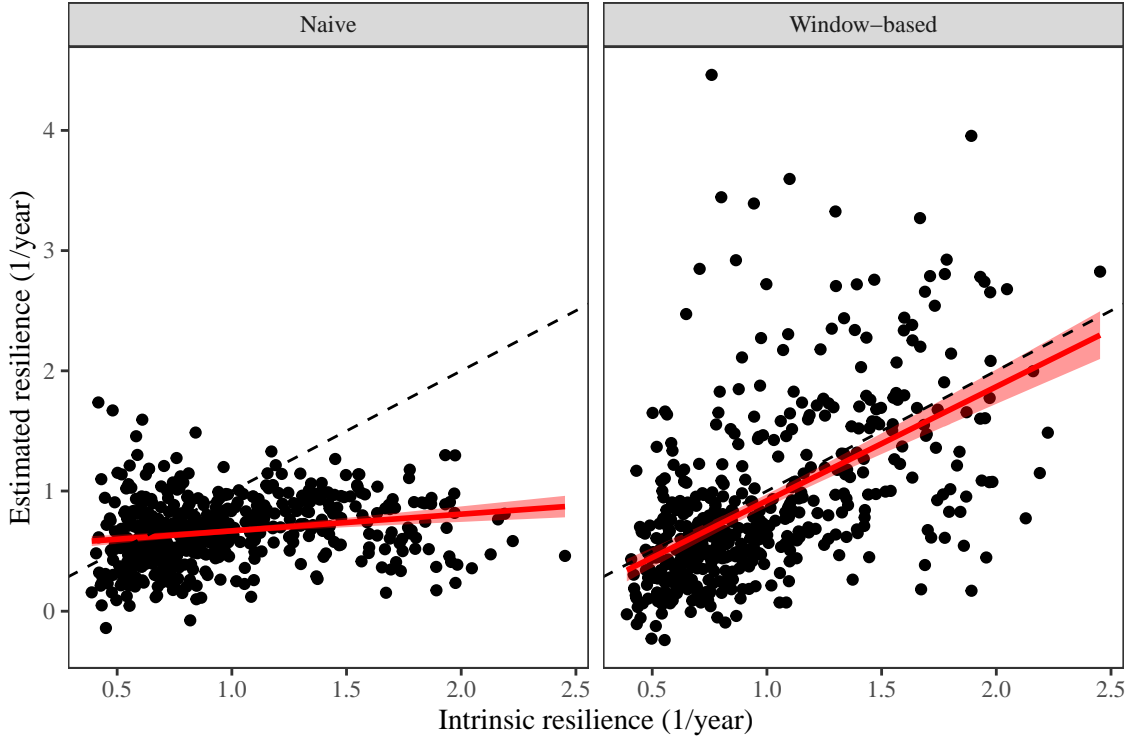


Figure S7: Impact of fitting window selection on the estimation of empirical resilience. We simulate 500 epidemics using stochastic SIRS model with randomly drawn parameters and randomly generated intervention impacts. For each simulation, we reconstruct the empirical attractor based on the approach outlined in Figure 3 and estimate the distance from attractor. The naive approach fits a linear regression on a log scale, starting from the maximum distance until the end of the time series. The window-based approach tries to select an appropriate window by smoothing the distance estimates and finding a time period when the smoothed time series crosses pre-determined threshold, relatively to the maximum distance; then, a linear regression is fitted by using the raw distance within this time period.

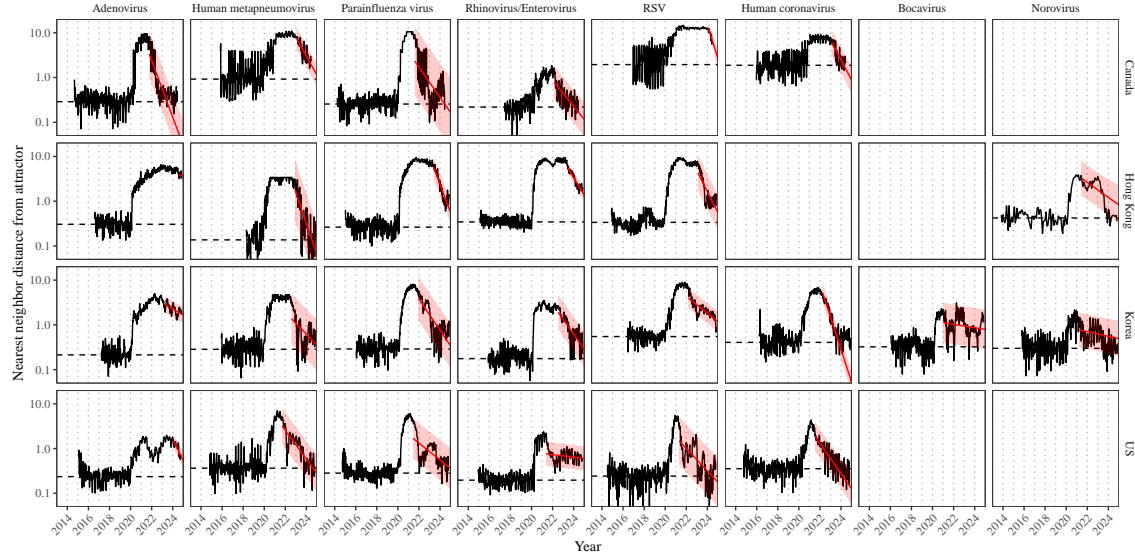


Figure S8: Estimated time series of distance from attractor for each pathogen across Canada, Hong Kong, Korea, and the US. Black lines represent the estimated distance from attractor. Red lines and shaded regions represent the linear regression fits and corresponding 95% confidence intervals. Dashed lines represent the average of the pre-pandemic nearest neighbor distances.

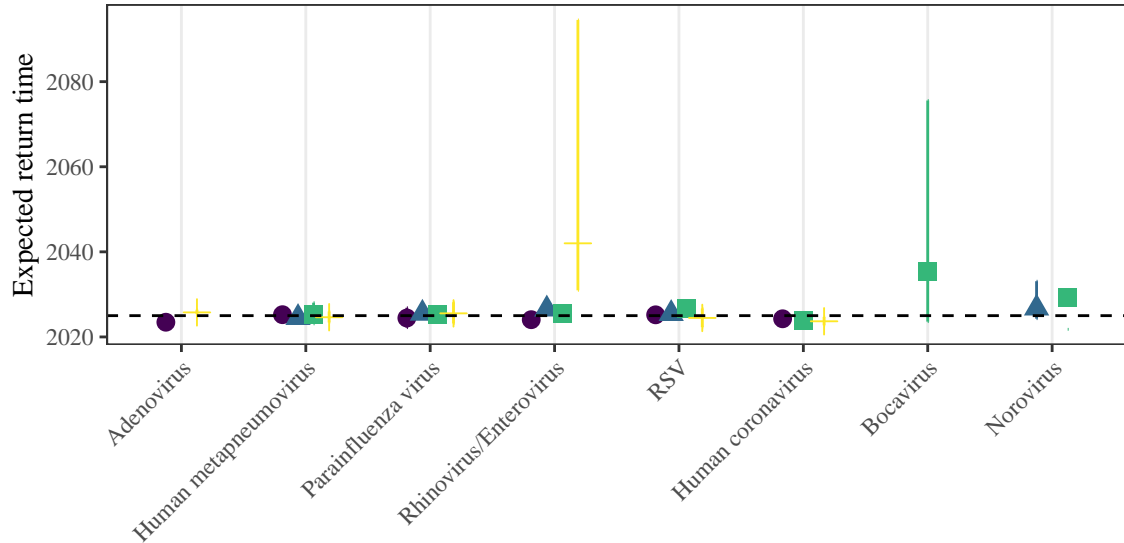


Figure S9: **Predicted timing of when each pathogen will return to their pre-pandemic cycles (zoomed out).** The dashed line in panel B indicates the end of 2024 (current observation time). Error bars represent 95% confidence intervals.

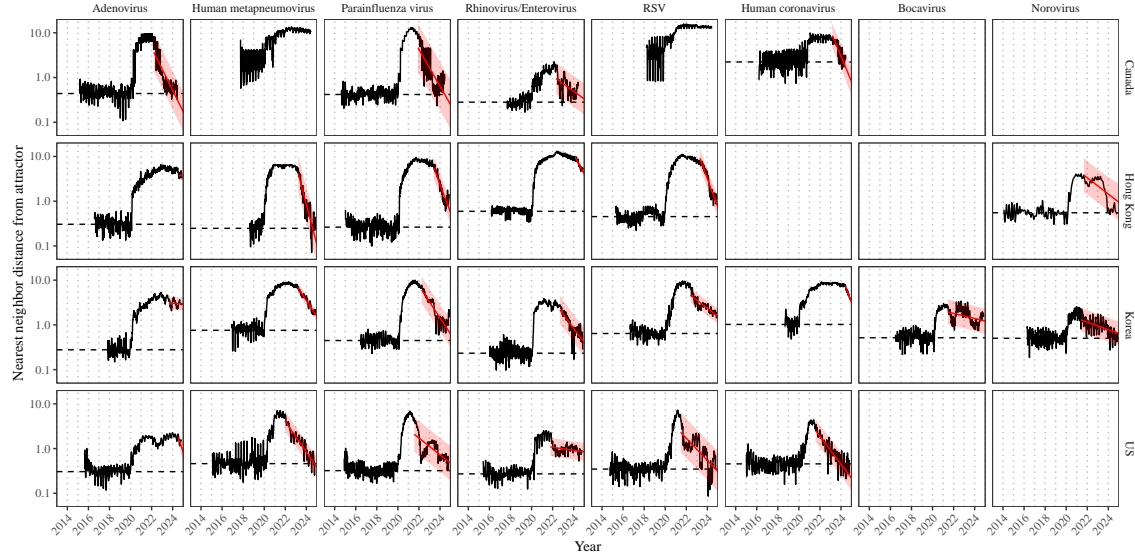


Figure S10: Estimated time series of distance from attractor for each pathogen across Canada, Hong Kong, Korea, and the US using higher embedding dimensions. Black lines represent the estimated distance from attractor. Red lines and shaded regions represent the linear regression fits and corresponding 95% confidence intervals. Dashed lines represent the average of the pre-pandemic nearest neighbor distances. A lower threshold is used for determining embedding dimensions with the false nearest neighbors approach, thereby yielding a higher embedding dimension.

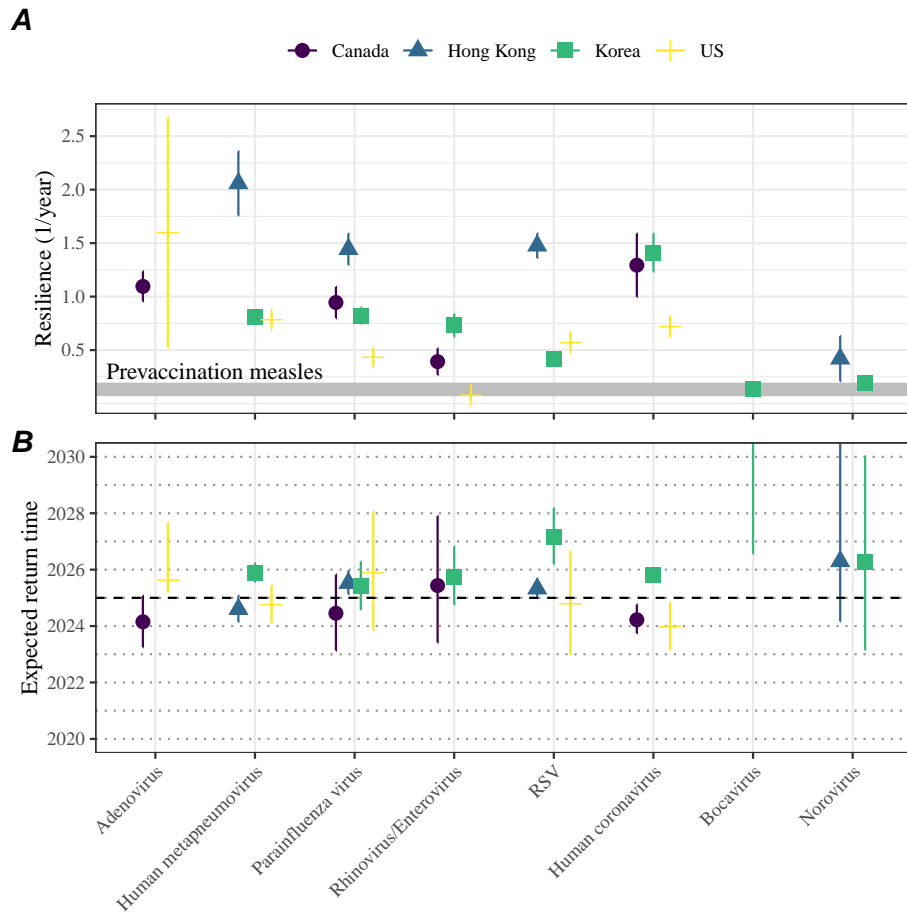


Figure S11: Summary of resilience estimates using higher embedding dimensions. (A) Estimated pathogen resilience. The gray horizontal line represents the intrinsic resilience of pre-vaccination measles dynamics. (B) Predicted timing of when each pathogen will return to their pre-pandemic cycles. The dashed line in panel B indicates the end of 2024 (current observation time). Error bars represent 95% confidence intervals. A lower threshold is used for determining embedding dimensions with the false nearest neighbors approach, thereby yielding a higher embedding dimension.

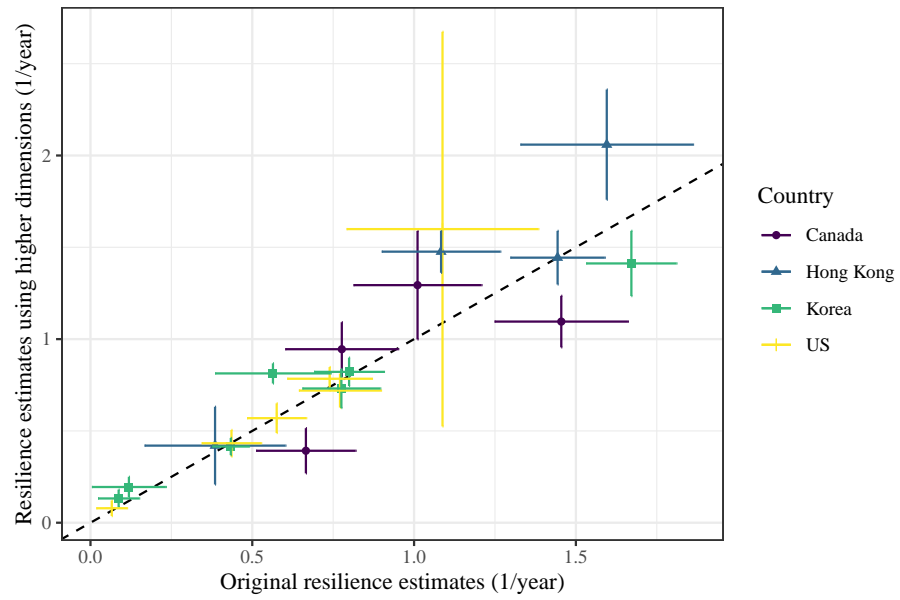


Figure S12: **Comparison of resilience estimates.** Each point represents a resilience estimate for a specific pathogen at a specific country. The x values represent the original resilience estimates presented in Figure 4. The y values represent the original resilience estimates presented in Supplementary Figure S11.

561 References

- 562 [1] Edward A Bender, Ted J Case, and Michael E Gilpin. Perturbation experiments
563 in community ecology: theory and practice. *Ecology*, 65(1):1–13, 1984.
- 564 [2] Anthony R Ives and Stephen R Carpenter. Stability and diversity of ecosystems.
565 *science*, 317(5834):58–62, 2007.
- 566 [3] Marten Scheffer, Jordi Bascompte, William A Brock, Victor Brovkin, Stephen R
567 Carpenter, Vasilis Dakos, Hermann Held, Egbert H Van Nes, Max Rietkerk,
568 and George Sugihara. Early-warning signals for critical transitions. *Nature*,
569 461(7260):53–59, 2009.
- 570 [4] Stuart L Pimm. The structure of food webs. *Theoretical population biology*,
571 16(2):144–158, 1979.
- 572 [5] Michael G Neubert and Hal Caswell. Alternatives to resilience for measuring
573 the responses of ecological systems to perturbations. *Ecology*, 78(3):653–665,
574 1997.
- 575 [6] Lance H Gunderson. Ecological resilience—in theory and application. *Annual
576 review of ecology and systematics*, 31(1):425–439, 2000.
- 577 [7] Vasilis Dakos and Sonia Kéfi. Ecological resilience: what to measure and how.
578 *Environmental Research Letters*, 17(4):043003, 2022.
- 579 [8] Jeanne C Chambers, Craig R Allen, and Samuel A Cushman. Operationalizing
580 ecological resilience concepts for managing species and ecosystems at risk.
581 *Frontiers in Ecology and Evolution*, 7:241, 2019.
- 582 [9] Rachel E Baker, Sang Woo Park, Wenchang Yang, Gabriel A Vecchi, C Jessica E
583 Metcalf, and Bryan T Grenfell. The impact of COVID-19 nonpharmaceutical
584 interventions on the future dynamics of endemic infections. *Proceedings of the
585 National Academy of Sciences*, 117(48):30547–30553, 2020.
- 586 [10] Gabriela B Gomez, Cedric Mahé, and Sandra S Chaves. Uncertain effects of the
587 pandemic on respiratory viruses. *Science*, 372(6546):1043–1044, 2021.
- 588 [11] Mihaly Koltai, Fabienne Krauer, David Hodgson, Edwin van Leeuwen, Marina
589 Treskova-Schwarzbach, Mark Jit, and Stefan Flasche. Determinants of RSV
590 epidemiology following suppression through pandemic contact restrictions. *Epi-
591 demics*, 40:100614, 2022.
- 592 [12] Sang Woo Park, Brooklyn Noble, Emily Howerton, Bjarke F Nielsen, Sarah
593 Lentz, Lilliam Ambroggio, Samuel Dominguez, Kevin Messacar, and Bryan T
594 Grenfell. Predicting the impact of non-pharmaceutical interventions against
595 COVID-19 on *Mycoplasma pneumoniae* in the United States. *Epidemics*,
596 49:100808, 2024.

- 597 [13] Eric J Chow, Timothy M Uyeki, and Helen Y Chu. The effects of the COVID-19
598 pandemic on community respiratory virus activity. *Nature Reviews Microbiology*,
599 21(3):195–210, 2023.
- 600 [14] Georgiy V Bobashev, Stephen P Ellner, Douglas W Nychka, and Bryan T
601 Grenfell. Reconstructing susceptible and recruitment dynamics from measles
602 epidemic data. *Mathematical Population Studies*, 8(1):1–29, 2000.
- 603 [15] Bärbel F Finkenstädt and Bryan T Grenfell. Time series modelling of childhood
604 diseases: a dynamical systems approach. *Journal of the Royal Statistical Society
605 Series C: Applied Statistics*, 49(2):187–205, 2000.
- 606 [16] Floris Takens. Detecting strange attractors in turbulence. In *Dynamical Sys-
607 tems and Turbulence, Warwick 1980: proceedings of a symposium held at the
608 University of Warwick 1979/80*, pages 366–381. Springer, 2006.
- 609 [17] Alan Hastings, Karen C Abbott, Kim Cuddington, Tessa Francis, Gabriel Gell-
610 ner, Ying-Cheng Lai, Andrew Morozov, Sergei Petrovskii, Katherine Scran-
611 ton, and Mary Lou Zeeman. Transient phenomena in ecology. *Science*,
612 361(6406):eaat6412, 2018.
- 613 [18] Matthew B Kennel, Reggie Brown, and Henry DI Abarbanel. Determining
614 embedding dimension for phase-space reconstruction using a geometrical con-
615 struction. *Physical review A*, 45(6):3403, 1992.
- 616 [19] Eugene Tan, Shannon Algar, Débora Corrêa, Michael Small, Thomas Stemler,
617 and David Walker. Selecting embedding delays: An overview of embedding
618 techniques and a new method using persistent homology. *Chaos: An Interdis-
619 ciplinary Journal of Nonlinear Science*, 33(3), 2023.
- 620 [20] Samit Bhattacharyya, Per H Gesteland, Kent Korgenski, Ottar N Bjørnstad,
621 and Frederick R Adler. Cross-immunity between strains explains the dynamical
622 pattern of paramyxoviruses. *Proceedings of the National Academy of Sciences*,
623 112(43):13396–13400, 2015.
- 624 [21] Bryan T Grenfell, Ottar N Bjørnstad, and Bärbel F Finkenstädt. Dynamics of
625 measles epidemics: scaling noise, determinism, and predictability with the TSIR
626 model. *Ecological monographs*, 72(2):185–202, 2002.
- 627 [22] Virginia E Pitzer, Cécile Viboud, Vladimir J Alonso, Tanya Wilcox, C Jessica
628 Metcalf, Claudia A Steiner, Amber K Haynes, and Bryan T Grenfell. Environ-
629 mental drivers of the spatiotemporal dynamics of respiratory syncytial virus in
630 the United States. *PLoS pathogens*, 11(1):e1004591, 2015.
- 631 [23] Katharine R Dean, Fabienne Krauer, Lars Walløe, Ole Christian Lingjærde, Bar-
632 bara Bramanti, Nils Chr Stenseth, and Boris V Schmid. Human ectoparasites

- 633 and the spread of plague in Europe during the Second Pandemic. *Proceedings*
634 *of the National Academy of Sciences*, 115(6):1304–1309, 2018.
- 635 [24] Margarita Pons-Salort and Nicholas C Grassly. Serotype-specific immunity
636 explains the incidence of diseases caused by human enteroviruses. *Science*,
637 361(6404):800–803, 2018.
- 638 [25] Sarah Cobey and Edward B Baskerville. Limits to causal inference with state-
639 space reconstruction for infectious disease. *PloS one*, 11(12):e0169050, 2016.
- 640 [26] Stephen M Kissler, Christine Tedijanto, Edward Goldstein, Yonatan H Grad,
641 and Marc Lipsitch. Projecting the transmission dynamics of SARS-CoV-2
642 through the postpandemic period. *Science*, 368(6493):860–868, 2020.
- 643 [27] Edward Goldstein, Sarah Cobey, Saki Takahashi, Joel C Miller, and Marc Lip-
644 sitch. Predicting the epidemic sizes of influenza A/H1N1, A/H3N2, and B: a
645 statistical method. *PLoS medicine*, 8(7):e1001051, 2011.